

# The mitochondrial calcium uniporter compensates for Complex I dysfunction

**Enrique Balderas**

University of Utah

**David Eberhardt**

University of Utah

**John Pleinis**

University of Utah

**Salah Sommakia**

University of Utah

**Anthony Balynas**

University of Utah

**Xue Yin**

University of Utah

**Sandra Lee**

University of Utah

**Mitchell Parker**

University of Nevada

**Colin Maguire**

University of Utah

**Scott Cho**

University of Utah

**Anna Bakhtina**

University of Utah

**Ryan Bia**

University of Utah

**Marisa Friederich**

University of Colorado

**Timothy Locke**

University of Washington <https://orcid.org/0000-0002-9177-7805>

**Johan Van Hove**

University of Colorado

**Stavros Drakos**

University of Utah

**Yasemin Sancak**

University of Washington <https://orcid.org/0000-0002-9328-7287>

**Martin Tristani-Firouzi**

University of Utah

**Sarah Franklin**

University of Utah

**Aylin Rodan**

University of Utah

**Dipayan Chaudhuri** (✉ [dipayan.chaudhuri@hsc.utah.edu](mailto:dipayan.chaudhuri@hsc.utah.edu))

University of Utah <https://orcid.org/0000-0003-0605-7334>

---

## Article

**Keywords:** Calcium (Ca<sup>2+</sup>), mitochondria, Complex I dysfunction

**Posted Date:** April 21st, 2021

**DOI:** <https://doi.org/10.21203/rs.3.rs-378028/v1>

**License:**   This work is licensed under a Creative Commons Attribution 4.0 International License.

[Read Full License](#)

---

**Version of Record:** A version of this preprint was published at Nature Communications on May 19th, 2022. See the published version at <https://doi.org/10.1038/s41467-022-30236-4>.

## The mitochondrial calcium uniporter compensates for Complex I dysfunction

Enrique Balderas [1], David R. Eberhardt [1], John M. Pleinis [2], Salah Sommakia [1], Anthony M. Balynas [1], Xue Yin [1], Sandra Lee [1], Mitchell C. Parker [3], Colin T. Maguire [4], Scott Cho [1], Anna Bakhtina [1], Ryan D. Bia [1], Marisa W. Friederich [5] [6], Timothy M. Locke [7], Johan L. K. Van Hove [5], Stavros G. Drakos [1] [8], Yasemin Sancak [7], Martin Tristani-Firouzi [1] [9], Sarah Franklin [1] [8], Aylin R. Rodan [2] [10], Dipayan Chaudhuri [1] [8] [11]

- [1] *Nora Eccles Harrison Cardiovascular Research and Training Institute, University of Utah, Salt Lake City, Utah, USA.*
- [2] *Molecular Medicine Program, University of Utah, Salt Lake City, Utah, USA.*
- [3] *University of Nevada, Reno School of Medicine, Reno, Nevada, USA.*
- [4] *Center for Clinical & Translational Sciences, University of Utah, Salt Lake City, Utah, USA.*
- [5] *Section of Clinical Genetics and Metabolism, Department of Pediatrics, University of Colorado, Aurora, Colorado, USA.*
- [6] *Department of Pathology and Laboratory Medicine, Children's Hospital Colorado, Aurora, Colorado, USA.*
- [7] *Department of Pharmacology, University of Washington, Seattle, Washington, USA.*
- [8] *Division of Cardiovascular Medicine, Department of Internal Medicine, University of Utah, Salt Lake City, Utah, USA.*
- [9] *Division of Pediatric Cardiology, University of Utah School of Medicine, Salt Lake City, Utah, USA.*
- [10] *Division of Nephrology and Hypertension, Department of Internal Medicine, University of Utah, Salt Lake City, Utah, USA.*
- [11] *Department of Biochemistry, Department of Biomedical Engineering, University of Utah, Salt Lake City, Utah, USA.*

Lead contact:

Dipayan Chaudhuri, MD, PhD  
Nora Eccles Harrison Cardiovascular Research and Training Institute  
University of Utah  
95 South 2000 East  
Building 500  
Salt Lake City, UT 84112  
[dipayan.chaudhuri@hsc.utah.edu](mailto:dipayan.chaudhuri@hsc.utah.edu)  
+1 (801) 585-3682

## ABSTRACT

**Calcium ( $\text{Ca}^{2+}$ ) entering mitochondria potently stimulates ATP synthesis. Increases in  $\text{Ca}^{2+}$  preserve energy synthesis in cardiomyopathies caused by mitochondrial dysfunction, and occur due to enhanced activity of the mitochondrial  $\text{Ca}^{2+}$  uniporter channel. The signaling mechanism that mediates this compensatory increase remains unknown. Here, we find that increases in the uniporter are due to impairment in Complex I of the electron transport chain (ETC). In normal physiology, Complex I promotes uniporter degradation via an interaction with the uniporter pore-forming subunit, a process we term Complex I-induced protein turnover (CLIPT). When Complex I dysfunction ensues, contact with the uniporter is inhibited, preventing degradation, and leading to a build-up in functional channels. Preventing uniporter activity leads to early demise in Complex I-deficient animals. Conversely, enhancing uniporter stability rescues survival and function in Complex I deficiency. Taken together, our data identify a fundamental pathway producing compensatory increases in  $\text{Ca}^{2+}$  influx during Complex I impairment.**

## INTRODUCTION

$\text{Ca}^{2+}$  is a potent regulator of metabolism, acting on multiple enzymes in mitochondria. Within the matrix, moderate  $\text{Ca}^{2+}$  elevations double ATP synthesis rates, helping match energetic supply to demand<sup>1, 2</sup>. Pathological failure to meet demand is a common feature across in cardiomyopathies. In fact, energetic failure can be a primary cause of cardiomyopathy in mitochondrial diseases. Such diseases involve deficient oxidative phosphorylation, and arise from mutations in mitochondrial proteins encoded by either the nuclear or the mitochondrial genome (mtDNA), with Complex I of the ETC most affected<sup>3, 4</sup>. Despite often severe pathology, children with mitochondrial cardiomyopathies may survive prolonged periods, suggesting mechanisms exist to compensate for ETC dysfunction. Identifying such pathways offers new opportunities for broad therapeutic intervention, as ETC impairment is a fundamental feature of many common cardiac and neurological diseases.

There are limited prior investigations of mitochondrial  $\text{Ca}^{2+}$  signaling during ETC deficiency<sup>5-11</sup>. The typical finding is reduced or unchanged  $\text{Ca}^{2+}$  uptake in the presence of a diminished membrane voltage gradient ( $\Delta\Psi$ ), where the diminished gradient correlated with severity of ETC deficiency. Because  $\text{Ca}^{2+}$  influx through the uniporter is driven by this voltage gradient, a change to either  $\Delta\Psi$  or uniporter activity can alter the size of  $\text{Ca}^{2+}$  influx. In ETC-deficient mitochondria, precisely such diminished  $\Delta\Psi$  may mask any compensatory increases in uniporter activity using typical *in vitro* imaging assays. In fact, we noted an interesting phenotype in mice with a cardiac-specific deletion of the transcription factor for mtDNA, *Tfam* (*transcription factor A, mitochondrial*). This is a well-established model for mitochondrial cardiomyopathies, featuring a dilated cardiomyopathy caused by impaired transcription of core mtDNA-encoded ETC subunits, with Complex I function most severely affected<sup>12, 13</sup>. Notably, as cardiomyopathy develops in the *Tfam* knockout, cardiac mitochondria become extremely  $\text{Ca}^{2+}$  avid, which may preserve ATP synthesis<sup>12</sup>. The increase in mitochondrial  $\text{Ca}^{2+}$  is mediated by a multi-subunit channel known as the mitochondrial  $\text{Ca}^{2+}$  uniporter<sup>14-20</sup>. This channel resides in the inner membrane of mitochondria, is activated by cytoplasmic  $\text{Ca}^{2+}$ , and is the main portal for  $\text{Ca}^{2+}$  entry into the matrix. In animal models, cardiac impairment of this channel leads to energetic supply-demand mismatch, leaving open the question of whether increased uniporter activity is an essential compensatory mechanism during ETC impairment.

Here, we unravel the mechanism for the enhancement in uniporter activity during ETC dysfunction and show that it is essential for survival. We find that this phenomenon depends on impairment in Complex I and is widespread, occurring in a variety of cell types, and across species. Under

normal Complex I activity, uniporter turnover is accelerated by an interaction between the N-terminal domain (NTD) of the pore-forming subunit of the uniporter (MCU) and Complex I, a mechanism we term *Complex I-induced protein turnover* (CLIPT). When Complex I becomes dysfunctional, CLIPT is abrogated, leading to slower MCU turnover and a buildup of uniporter channels. This mechanism is evident in hearts from *Tfam* knockout mice, and its disruption leads to their faster demise. Similarly, in *Drosophila*,  $\text{Ca}^{2+}$  signaling through the uniporter is essential for survival during Complex I dysfunction. Enhancing this mechanism, by overexpression of MCU or its NTD, in Complex I deficient flies rescues both functional impairments and survival.

## RESULTS

### Complex I dysfunction leads to enhanced mitochondrial calcium uniporter levels.

Measuring  $\text{Ca}^{2+}$  uptake using typical  $\text{Ca}^{2+}$  fluorescence assays poorly captures uniporter activity during ETC dysfunction, because such dysfunction also alters other parameters controlling  $\text{Ca}^{2+}$  transport, including  $\Delta\Psi$ , pH, morphology, and  $\text{Ca}^{2+}$  buffering<sup>8, 21, 22</sup>. To more precisely examine uniporter-mediated  $\text{Ca}^{2+}$  uptake, we used whole-mitoplast voltage-clamp electrophysiology<sup>17</sup>. In this assay, micropipettes are attached to individual spherical mitoplasts (mitochondria stripped of their outer membranes) to record ionic currents through a voltage-clamp feedback electrode. This allows full control over  $\Delta\Psi$ , matrix and external solutions, eliminating uncontrolled variation in the factors listed, and allowing direct measurement of uniporter  $\text{Ca}^{2+}$  currents ( $I_{\text{MiCa}}$ ).

The complexes with *Tfam*-dependent subunits (Complexes I, III, and IV) may integrate into a supercomplex known as the respirasome. Therefore, we first tested whether enhanced  $I_{\text{MiCa}}$  depended on disrupting the respirasome or a specific ETC complex. We examined HEK293T cells because long-term culture with drugs is possible, gene-edited lines exist for both uniporter<sup>23</sup> and Complex I analysis<sup>24</sup>, and uniporter currents are robust<sup>15</sup>. Individual ETC Complexes were inhibited pharmacologically for 2-3 days in HEK293T cells. To maintain viability, cells were cultured with 0.4 mM uridine to maintain pyrimidine biosynthesis and 2 mM pyruvate to regenerate  $\text{NAD}^+$ <sup>25, 26</sup>. Whereas chronic inhibition with Complex III or IV antagonists (1  $\mu\text{M}$  antimycin A, 200  $\mu\text{M}$  sodium azide) produced no change in  $I_{\text{MiCa}}$  (Fig. S1a, b), disruption of Complex I with rotenone produced a dose-dependent increase in  $I_{\text{MiCa}}$  (Fig. 1a, b). Rotenone did not alter channel kinetics, and failed to increase  $I_{\text{MiCa}}$  when added during mitoplast recordings (Fig. S1c, d). This suggests that rotenone did not enhance  $I_{\text{MiCa}}$  directly, but through its effect on Complex I, by inhibiting electron transfer to ubiquinone. Similar to the effect in *Tfam* knockout hearts<sup>12</sup>, protein levels for uniporter subunits MCU and EMRE were increased (Fig. 1c), though gene expression was not (relative gene expression MCU,  $0.89 \pm 0.18$ ; EMRE,  $1.37 \pm 0.4$ ; MICU1,  $1.03 \pm 0.15$ ,  $n = 3$ ).

Having established that the increase in uniporter currents observed in *Tfam* knockout cardiomyocytes could be reproduced by isolated Complex I inhibition, we tested the robustness of this phenomenon. To confirm the increase in  $I_{\text{MiCa}}$  was due to Complex I and not an off-target rotenone effect, we measured  $I_{\text{MiCa}}$  in HEK293T cells featuring deletion of the Complex I accessory subunit NDUFB10 or late assembly factor FOXRED1 (NDUFB10<sup>KO</sup>, FOXRED1<sup>KO</sup>, Fig. S1e)<sup>24, 27</sup>. In these,  $I_{\text{MiCa}}$  was also substantially increased over controls (Fig. 1d, e). We saw a similar increase in  $I_{\text{MiCa}}$  after disruption of accessory subunit NDUF54, which produces much milder Complex I deficiency (Fig. S1f)<sup>10, 24</sup>, suggesting that even limited Complex I impairment can activate this mechanism. To see if  $I_{\text{MiCa}}$  enhancement was prevalent in Complex I-mediated disease, we obtained fibroblasts from an infant with fatal lactic acidosis and cardiomyopathy due to NDUFB10 deficiency (NDUFB10<sup>-C107S</sup>)<sup>28</sup>. Induced pluripotent stem cells (iPSCs) derived from these fibroblasts retained the compound heterozygous mutations and had essentially absent NDUFB10

expression (Fig. S1g-i), validating their use for gauging uniporter activity in Complex I-deficient disease.  $I_{\text{MiCa}}$  in these cells was also increased, and this effect was rescued by re-expression of wild-type NDUFB10 (Fig. 1f). Next, to see if this effect was evolutionarily conserved, we examined *Drosophila* with Complex I dysfunction in flight muscle, generated by the expression of short hairpin RNA (shRNA) targeting NDUFB10 via *MHC*-Gal4 (NDUFB10<sup>RNAi</sup>)<sup>29</sup>. Here too Complex I dysfunction was associated with an increase in  $I_{\text{MiCa}}$  (Fig. 1g). Of note, matrix free  $[\text{Ca}^{2+}]$  levels were higher in the Complex I deficient cells (Fig. S1j), though there was substantial overlap with controls. Thus, one main purpose of enhancing  $I_{\text{MiCa}}$  may be to maintain mitochondrial  $\text{Ca}^{2+}$  levels when dysfunctional Complex I leads to a depolarized mitochondrial membrane potential and blunted  $\text{Ca}^{2+}$  uptake through individual channels. Finally, we confirmed that the increase in current was specific to the uniporter, as the chloride current carried by the ubiquitous inner membrane anion channel showed no change after rotenone incubation in HEK293T cells (Fig. S1k). In summary, we show that disrupting Complex I leads to an approximately 2-3 fold increase in  $I_{\text{MiCa}}$ . This effect can be triggered by a variety of insults to Complex I (*Tfam* knockout, rotenone, gene editing, shRNA, and congenital mutations), and occurs across species (mouse, *Drosophila*, human), cell types (cardiomyocytes, flight muscle, cultured lines, and iPSCs), and in human disease.

As with the *Tfam* knockout mice<sup>12</sup> and the rotenone-treated HEK293T cells, NDUFB10<sup>KO</sup>, FOXRED1<sup>KO</sup>, and NDUFB10<sup>-C107S</sup> cells also exhibited increased MCU protein, suggesting that the enhancement in  $I_{\text{MiCa}}$  reflects an increase in channels (Fig. 1c). MCU levels increased in these different lines despite the absence of a corresponding mRNA upregulation (MCU expression versus control: 0.95, NDUFB10<sup>KO</sup>; 0.68, FOXRED1<sup>KO</sup>; 0.88, NDUFB10<sup>-C107S</sup>,  $n = 2$ ). The discordance between MCU protein and mRNA levels may be explained by a post-transcriptional mechanism. To further verify this, we expressed carboxy-terminal Flag-tagged MCU in MCU<sup>KO</sup> HEK293T cells from a plasmid lacking the native promoter, introns, and other untranslated regions, disrupting endogenous transcriptional regulation<sup>23</sup>. Here too we found that  $I_{\text{MiCa}}$  increased after rotenone incubation (Fig. 1h). Thus, our results suggest Complex I regulation of the uniporter is post-transcriptional.

### **Aberrant NAD<sup>+</sup>/NADH oxidation and reactive oxygen species (ROS) production drive uniporter enhancement.**

Next, we investigated the signal that leads to  $I_{\text{MiCa}}$  enhancement. When Complex I becomes dysfunctional, its NADH:ubiquinone oxidoreductase activity is impaired, leading to an increased NADH:NAD<sup>+</sup> ratio and greater superoxide production, which persist until excess ROS leads to self-inactivation and Complex I disassembly (Fig. 2a)<sup>30, 31</sup>. We found evidence for increases in superoxide production using the mitochondrially-targeted sensor MitoSOX, and increased NADH:NAD<sup>+</sup> ratio using a mitochondrially-targeted version of the genetically-encoded SoNar sensor (Fig. 2b, c)<sup>32</sup>. To test if these were key signals for  $I_{\text{MiCa}}$  enhancement, we turned again to whole-mitoplast electrophysiology. To blunt changes in the NADH:NAD<sup>+</sup> ratio, cell lines were engineered to stably express a mitochondrially-targeted water-forming NADH oxidase from *Lactobacillus brevis* (*LbNOX*, Fig. S2a). This approach was previously shown to reduce NADH/NAD<sup>+</sup> ratios during Complex I inhibition<sup>25</sup>.  $I_{\text{MiCa}}$  magnitudes from *LbNOX*-expressing cells were no longer increased following rotenone treatment, suggesting that abnormal NADH oxidation contributes to uniporter enhancement (Fig. 2d).

Employing a similar strategy to blunt the increase in superoxide, we generated cells stably overexpressing *mitochondrial superoxide dismutase 2* (SOD2, Fig. S2b). In these cells, baseline and rotenone-induced superoxide production was blunted (Fig. S2d).  $I_{\text{MiCa}}$  also failed to increase

following rotenone treatment (Fig. 2e). We then tested the reciprocal hypothesis, that producing ROS would be sufficient to induce  $I_{\text{MiCa}}$  enhancement. A cell line was created stably expressing a mitochondria-targeted version of mini-singlet oxygen generator (mt-miniSOG, Fig. S2c). This fluorescent flavoprotein generates singlet oxygen when excited by blue light, and substantially increased production of superoxide (Fig. S2e)<sup>33</sup>. In cells exposed to blue light 2-3 days before recording,  $I_{\text{MiCa}}$  size was  $\sim 3\times$  greater than in unexposed cells (Fig. 2f).

Mito-*LbNOX* has been used to rescue cell survival by preserving NADH:NAD<sup>+</sup> homeostasis during dysfunction induced by the Complex I inhibitor piericidin<sup>25</sup>. Thus, to determine whether maintaining NADH:NAD<sup>+</sup> homeostasis during Complex I impairment required the uniporter, we expressed mito-*LbNOX* in control and MCU<sup>KO</sup> HEK293T and exposed them to 500 nM piericidin. In control cells, mito-*LbNOX* expression did not alter cell survival and partially rescued the cell proliferation defect caused by piericidin, as expected (Fig. S2f). In contrast, expressing mito-*LbNOX* in MCU<sup>KO</sup> cells both impaired baseline cell survival and failed to rescue cell death after piericidin treatment, suggesting that the uniporter boosting of NADH:NAD<sup>+</sup> is required for survival during Complex I dysfunction. Taken together, these data indicate that aberrant NADH oxidation and ROS generation are critical signals for uniporter enhancement during Complex I dysfunction.

### **The MCU N-terminal domain is necessary for Complex-I mediated enhancement.**

In a prior report, MCU was shown to be sensitive to matrix redox status and oxidative stress via S-glutathionylation at a conserved cysteine residue in its N-terminal domain (NTD)<sup>34</sup>. Though such regulation was not specific to Complex I, it offered a potential mechanism to explain  $I_{\text{MiCa}}$  enhancement. Therefore, we expressed an MCU construct where all five cysteines were mutated (Cysteine-free MCU, CF-MCU) in MCU<sup>KO</sup> cells. As in the prior report, CF-MCU conducted  $I_{\text{MiCa}}$ , with no obvious effect on basal channel function. Unexpectedly, rotenone-mediated  $I_{\text{MiCa}}$  enhancement persisted in these cells (Fig. S2g). These data indicate that redox sensation by MCU cysteines fails to explain uniporter enhancement observed during Complex I dysfunction.

Nevertheless, the MCU NTD itself remained an interesting target to examine further. This structure is evolutionarily conserved, forming an independent domain within the matrix<sup>35-37</sup>. The NTD has been implicated in channel dimerization, though it is not essential for channel activity<sup>35, 36</sup>. Given its highly-conserved structure, we hypothesized that the NTD may be responsible for Complex I-mediated enhancement. MCU lacking the NTD ( $\Delta$ NTD-MCU) was stably expressed in MCU<sup>KO</sup> cells. Consistent with our hypothesis,  $I_{\text{MiCa}}$  in these cells failed to increase in response to rotenone (Fig. 2g). Thus, an intact MCU NTD is necessary for the enhancement in current seen during Complex I dysfunction.

### **Uniporter enhancement depends on an interaction between MCU and Complex I**

The importance of ROS in  $I_{\text{MiCa}}$  enhancement revealed an intriguing discrepancy. Complex III inhibition with antimycin A produces abundant ROS within the matrix and intermembrane space<sup>38</sup>, yet it did not lead to  $I_{\text{MiCa}}$  enhancement. We surmised that aberrant ROS may be primarily disrupting Complex I, and Complex I dysfunction subsequently altering uniporter behavior, which predicts close proximity between MCU and Complex I. Evidence for such an interaction was found incidentally in a proteomic screen for Complex I assembly factors, where MCU (annotated as *CCDC109A*) bound Complex I without affecting its assembly<sup>39</sup>. Similarly, a more recent compendium of mitochondrial protein-protein interactions revealed close proximity between MCU and several subunits of Complex I<sup>40</sup>. We therefore tested for a Complex I-MCU interaction. Immunoprecipitation of Flag-tagged MCU in 1% digitonin was followed by mass spectrometric analysis of co-precipitating proteins, identifying NDUFA3, NDUFA8, and NDUFA13 as potential

interactors (Fig. S3a). All three of these are closely apposed on the Complex I structure. We confirmed this interaction by co-immunoprecipitating NDUFA13 with MCU-Flag but not Flag-tagged succinate dehydrogenase complex subunit B (SDHB-Flag) (Fig. 3a).

To confirm the interaction within live cells with intact mitochondria, we turned to Förster energy resonance transfer (FRET) assays. For the mVenus-mCerulean pair used here, the Förster radius for 50% FRET efficiency is  $\sim 5$  nm<sup>41</sup>. We took advantage of prior studies that showed that several Complex I subunits, typically those that had carboxy-termini exposed at the Complex I surface, are unaffected by carboxy-terminal fusion with fluorescent proteins<sup>42</sup>. MCU can similarly be linked at its C-terminus with fluorescent proteins<sup>34</sup>. To sample various portions of Complex I, we tagged eight NDUF subunits with mVenus, while MCU was fused to mCerulean. FRET was detected from co-transfected constructs in HEK293T cells using flow cytometry, which allows us to measure interactions over a wide range of protein expression levels<sup>43</sup>. NDUFA2 and NDUFA5 failed to target mitochondria when tagged with mVenus, and reassuringly showed no FRET with MCU-mCerulean (Fig. 3b). Expressing mitochondria-targeted mVenus with MCU-mCerulean revealed that some FRET was detected at high mVenus concentrations. Such concentration-dependent effects likely reflect the small volume of the matrix relative to cytoplasm. This FRET level served as the bound for spurious interactions, and a similar value was seen for NDUFA7, NDUFB6, NDUFS6, and NDUFV2, suggesting that these either were distant from MCU or had fluorophore orientations that minimized FRET. NDUFA10 and NDUFS3, however, demonstrated robust interaction with MCU-mCerulean, implying close physical proximity.

Although our biochemical and FRET assays showed MCU-Complex I interaction, these required heterologous expression of tagged proteins. To confirm such interaction between endogenous molecules, we used the Duolink proximity ligation system, which stochastically produces bright fluorescent spots when target proteins less than  $\sim 40$  nm apart are co-immunolabeled<sup>44</sup>. We used anti-MCU and anti-NDUFS2 monoclonal antibodies to label the uniporter and Complex I respectively in HEK293T cells and iPSCs. Controls with either antibody alone, or in MCU<sup>KO</sup> cells, displayed no Duolink spots (Fig. S3b, c). When both antibodies were used, we saw robust Duolink labeling ( $3.6 \pm 0.3$  spots/cell, Fig. 3c). To confirm the interaction, we took advantage of the more lenient distance threshold detected by the Duolink system and used an antibody targeting Complex IV (MTCO1), since this is also part of the respirasome. This antibody also produced substantial, though less robust, Duolink signal, possibly because it is further from the putative MCU interaction site ( $2.8 \pm 0.5$  spots/cell, Fig. 3c, Fig. S3d). To show that the interaction was specific, we also performed the Duolink assay targeting Complex V (ATP5A), which is not part of the respirasome, and found substantially reduced labeling ( $0.7 \pm 0.2$  spots/cell).

Having established that endogenous Complex I interacts with MCU, we investigated changes produced by Complex I dysfunction. Treating HEK293T cells with rotenone eliminated NDUFA13-MCU co-immunoprecipitation and markedly reduced Duolink targeting ( $0.6 \pm 0.1$  spots/cell, Fig. 3a, c). Similarly, the NDUFB10<sup>-C107S</sup> iPSCs had diminished labeling compared to control (Control:  $3.5 \pm 0.1$  spots/cell, NDUFB10<sup>-C107S</sup>:  $1.4 \pm 0.1$  spots/cell), despite preserved NDUFS2 and MCU (Fig. 3d, Fig. S3e). In sum, based on immunoprecipitation, FRET, and proximity ligation, in both HEK293T cells and iPSCs, we find that MCU interacts with Complex I, but becomes decoupled when Complex I dysfunction ensues. Interestingly, an unexpected result from these assays was that the MCU-interacting NDUF subunits all clustered on the lateral surface of Complex I (Fig. S3f, g). This is consistent with the architecture of the respirasome, since MCU would not be hindered by the Complex III dimer nor Complex IV, which reside on the opposite sides. Taken together, we establish an interaction between MCU and Complex I that is disrupted during Complex I dysfunction.

## Complex I-dependent protein turnover (CLIPT) controls MCU degradation

A common finding in the multiple systems examined was an increase in uniporter protein consistent with enhanced  $I_{\text{MiCa}}$  (Fig. 1c). Such increases could be mediated by either enhanced synthesis or diminished degradation. The absence of mRNA upregulation and the ability to enhance  $I_{\text{MiCa}}$  in heterologously-expressed channels suggested the effect was likely not from greater synthesis. To evaluate MCU degradation, we designed a tetracycline-repressible MCU-Flag construct and expressed it in  $\text{MCU}^{\text{KO}}$  cells<sup>45</sup>. Cells were grown in 3% fetal bovine serum-supplemented media, to minimize proliferation. Addition of 1  $\mu\text{g}/\text{mL}$  doxycycline suppresses MCU-Flag transcription, leading to depletion within two days in control cells. In contrast, upon treatment with rotenone, MCU-Flag expression persisted for the four-day experimental timeline (Fig. 4a), confirming that reduced degradation of the uniporter was the primary mechanism for this effect. Inhibition of Complex III or IV produced no such effect on MCU. To confirm that stabilization was specific to MCU, we looked at another mitochondrial transmembrane protein regulated by ROS, ROMO1, and found that its lifetime failed to enhance after Complex I inhibition (Fig. S4a).

At this stage, we considered two potential hypotheses linking ROS production in Complex I to stabilization of MCU (Fig. S4b). The first, analogous to the cysteine mechanism described previously<sup>34</sup>, would involve post-translational modification (PTM) of a specific NTD residue that increases MCU stability (PTM hypothesis). Although simple, concerns about this hypothesis include the promiscuous modifications ROS can induce on target peptides. Many of these are irreversible, and tend to damage rather than enhance protein activity. Moreover, while ROS leaks from Complex I under physiological conditions, excess ROS produced during Complex I dysfunction induces self-inactivation<sup>30, 31</sup>. Excess ROS produced by mito-miniSOG is also more likely to non-specifically damage Complex I, which has large matrix components and is quite sensitive to indiscriminate ROS production, than produce a specific modification on MCU. Finally, Complex I impairment decouples MCU, and it is unclear how the ROS signal would modify channels no longer bound. Thus, we considered an alternate hypothesis, termed Complex I induced protein turnover (CLIPT). Here, under normal conditions MCU, via its NTD, interacts with Complex I to serve as a “ROS buffer”, being turned over by quality-control proteases as oxidative damage from basal ROS leakage impairs MCU function. When Complex I becomes dysfunctional from excess ROS, MCU can no longer interact and buffer ROS, becoming more stable.

To distinguish the PTM and CLIPT mechanisms, we first assayed how depleting quality-control proteases would affect MCU stability. Under the PTM hypothesis, this should not affect MCU stability, as there should be little ROS-induced damage. Conversely, if MCU is buffering Complex I ROS, impairing quality control will stabilize MCU. We depleted several quality-control proteases using shRNA, and found that LONP1 depletion led to an increase in MCU stability (Fig. S4c; % knockdown by qPCR: 0.88, AFG3L2; 0.89, CLPP; 0.93 LONP1; 0.88, SPG7,  $n = 2$ ). LONP1 performs quality control of matrix proteins, and this effect is consistent with modifications of matrix-resident NTD leading to quality control, rather than transmembrane domain quality-control proteases AFG3L2 and SPG7. Moreover, a close interaction between LONP1 and MCU was also detected in the recently published mitochondrial protein-protein compendium<sup>40</sup>. Next, we examined how the NTD affected stability. Expressing the NTD fragment by itself should have no effect on MCU stability under basal conditions for the PTM hypothesis, whereas excess NTD should disrupt the MCU-Complex I interaction and stabilize the channel during CLIPT. We expressed an HA-tagged NTD fragment in cells also containing doxycycline-repressible MCU-Flag, and found that MCU stability increased, consistent with CLIPT (Fig. 4b).

To further confirm CLIPT, we designed the drug-induced dimerization experiment outlined in Fig. 4c. The FK506-binding protein (FKBP) binds the FKBP-rapamycin-binding domain (FRB) of MTOR only in the presence of rapamycin<sup>46</sup>, and using this system allows us to determine if MCU-Complex I interaction is the key determinant of MCU stability, without having to create Complex I dysfunction. The MCU NTD was replaced with the similarly-sized FRB fragment, to generate a FRB-MCU fusion construct (Fig. 4d). For Complex I, we fused FKBP to NDUFA10 (NDUFA10-FKBP), the Complex I subunit showing strong FRET with MCU (Fig. 3b). As a control, we created a mitochondrially-targeted FKBP (mito-FKBP). First, we established that the system was functional. In MCU<sup>KO</sup> cells, FRB-MCU was able to confer Ca<sup>2+</sup> uptake (Fig. S4d), showing this construct formed functional channels. In the absence of rapamycin, FRB-MCU and the FKBP constructs failed to interact (Fig. 4e), confirming the importance of the NTD in MCU-Complex I binding, whereas adding 100 nM rapamycin induced robust co-immunoprecipitation.

Having established functional rapamycin-induced interaction, we used the tetracycline-repressible system to examine if MCU turnover depended on its Complex I interaction (Fig. 4f). 100 nM rapamycin was added to cell culture dishes one day prior to adding doxycycline to repress FRB-MCU transcription. When co-expressed with mito-FKBP, FRB-MCU showed minimal degradation in the presence or absence of rapamycin. Similarly, when co-expressed with NDUFA10-FKBP, FRB-MCU protein was stable in the absence of rapamycin. Remarkably, however, when rapamycin was added in this condition, FRB-MCU was rapidly degraded. Four implications arise from these results. First, the changes in MCU turnover are due to its interaction with Complex I, and not an off-target rotenone effect. Second, whereas a large fraction of full-length MCU degraded over 2 days under control conditions (Fig. 4a), removing the NTD conferred stability on the channel (Fig. 4f). Third, MCU turnover due to Complex I is not dependent on a specific modification of any particular NTD residue, since we could alter turnover in channels with the NTD replaced. Finally, MCU turnover appears to be tunable. Whereas enhancing the MCU-Complex I interaction with the FKBP-FRB-rapamycin system led to rapid MCU degradation, overexpressing the NTD alone stabilized it. Taken together, our results identify a new mechanism, Complex I induced protein turnover (CLIPT), critical for controlling uniporter levels and activity.

### **Uniporter stabilization during ETC impairment prolongs survival in mitochondrial cardiomyopathies**

Multiple studies over two decades have revealed that cardiac *Tfam* deletion in mice produces many of the same clinical, biochemical, and ultrastructural features found in human mitochondrial cardiomyopathies<sup>47-50</sup>. Therefore, to examine whether uniporter stability is enhanced *in vivo* during disease, we turned to this model. For cardiac-specific deletion, we use the *Myh6-Cre* recombinase driver, which begins expressing embryonically<sup>51</sup>. When crossed with *Tfam*<sup>loxP/loxP</sup> animals, loss of myocardial TFAM leads to a 75% reduction in Complex I activity, with 30-35% inhibition of Complex III and IV, and early death between 3-6 weeks of age<sup>12</sup>.

By crossing *Myh6-Cre* with *Mcu*<sup>loxP/loxP</sup> mice (*Mcu* KO), we could disrupt transcription of the *Mcu* gene, and assess its stability in *Mcu* KO, compared to mice with both *Mcu* and *Tfam* deleted (*Myh6-Cre*; *Tfam*<sup>loxP/loxP</sup>; *Mcu*<sup>loxP/loxP</sup> [*Tfam-Mcu* DKO]). By assaying for MCU protein persistence subsequent to Cre-mediated disruption of the *Mcu* gene, we could perform an *in vivo* experiment analogous to the transcriptional repression assays performed in cells (Fig. 4a). 10-14 day old mouse hearts were processed by Western blotting. Notably, despite embryonic initiation of *Mcu* deletion, we could detect substantial levels of uniporter subunit proteins in *Tfam-Mcu* DKO animals, approaching those seen in wild-type animals, compared with much lower levels in *Mcu* KO hearts (Fig. 5a). This result suggests that, although its transcription has been disrupted, the

MCU protein already present becomes much more stable in the ETC-deficient animals, compared to those with a functional ETC. This was not due to deficient Cre activity in the *Tfam-Mcu* DKO, as protein levels of TFAM were equally reduced between *Tfam* KO and *Tfam-Mcu* DKO hearts (Fig. 5a), *Tfam* mRNA transcripts were equally reduced between *Tfam* KO and *Tfam-Mcu* DKO hearts, and *Mcu* mRNA transcripts were equally reduced between *Mcu* KO and *Tfam-Mcu* DKO hearts (Fig. 5b). Moreover, this was also not due to MCU protein from excess infiltration of fibroblasts or other non-cardiac cells into the myocardium. Non-cardiomyocyte cell quantities are lowest in juvenile hearts, and their mitochondrial mass per cell is far smaller than in cardiomyocytes, demonstrated by the trivial amount of TFAM left after its deletion (Fig. 5a). A fibroblast marker, vimentin, was no different across the different genotypes (Fig. 5a). We also directly quantified cell amounts in histological slices. CellProfiler software was used to count the number of cellular nuclei in tissue slices from Masson's trichrome-stained hearts. *Mcu* KO and *Tfam-Mcu* DKO hearts had similar numbers of nuclei per mm<sup>2</sup> of tissue, these tended to be lower compared to wild-type animals, and no obvious excess non-cardiomyocyte infiltrates were noted (Fig. S5a, b). Therefore, as in cultured cells, disruption of the ETC *in vivo* in mouse myocardium led to increased stability of the uniporter.

To determine if these persistent uniporter channels were functional, we measured Ca<sup>2+</sup> uptake in mitochondrial fractions isolated from mouse hearts. We used fluorescent Ca<sup>2+</sup> imaging, as this allows an integrative assessment of Ca<sup>2+</sup> uptake in the context of TFAM deletion. Decreasing Oregon Green BAPTA 6F fluorescence following a Ca<sup>2+</sup> pulse indicated mitochondrial Ca<sup>2+</sup> uptake (Fig. 5c). Because TFAM deletion alters the driving force for Ca<sup>2+</sup> uptake, we quantified the steady-state ability of mitochondria to take up Ca<sup>2+</sup> rather than uptake rates (Fig. 5d). Wild-type mice took up the Ca<sup>2+</sup> pulse rapidly, whereas *Mcu* KO mice were unable to take up Ca<sup>2+</sup>, consistent with loss of functional uniporter. Most of the *Tfam-Mcu* DKO mice, however, had persistent Ca<sup>2+</sup> uptake, revealing preservation of functional uniporter channels, despite deletion of the *Mcu* gene.

Next, we assessed if loss of MCU impaired the health of *Tfam-Mcu* DKO mice. Of note, though MCU levels and activity persisted in the juvenile mice, as noted above, these were not at wild-type levels (Fig. 5a, d). Moreover, during the second postnatal week there appeared to be a reduction in the persistent uniporter channels, as a subset of *Tfam-Mcu* DKO mice were no longer capable of cardiac mitochondrial Ca<sup>2+</sup> uptake (lower points in Fig. 5d). Thus, we were still able to assess how partial depletion of MCU altered cardiac status. The *Tfam-Mcu* DKO developed a cardiomyopathy similar to *Tfam* KO mice. They had enlarged hearts (Fig. 5e), with reduced contractile function, dilated ventricles, and thinned walls on echocardiography (Fig. S5c-f). Remarkably, even partial loss of uniporter channels proved fatal, as a steep decline in survival occurred during the second postnatal week (Fig. 5f), with *Tfam-Mcu* DKO mice dying 1.5 weeks earlier than *Tfam* KO mice (survival time in weeks, average [95% confidence interval]: *Tfam-Mcu* DKO, 3.2 [2.9-3.5]; *Tfam* KO, 4.8 [4.5-5.0]). In summary, in a disease model of cardiac ETC dysfunction, activity of the uniporter was essential for survival.

### **NTD overexpression improves survival and function in Complex I-impaired *Drosophila***

Complex I deficiency is the most common cause of monogenic mitochondrial disorders, and is frequently implicated in neurological and cardiac disease<sup>52</sup>. To further explore the physiological relevance of the MCU-Complex I interaction. *Drosophila* is an ideal system, as models for Complex I disease exist<sup>29</sup>, the mitochondrial Ca<sup>2+</sup> uptake machinery is closely conserved<sup>53</sup>, and crosses can be rapidly generated. For these analyses, Complex I was inhibited in *Drosophila* flight muscle, which possesses sarcomeric organization and mitochondrial Ca<sup>2+</sup> uptake that mimics mammalian cardiomyocytes<sup>54</sup>. Complex I dysfunction in NDUFB10<sup>RNAi</sup> led to mild developmental

lethality and weak flies (Fig. 6a, b). To test flight muscle, the time it takes *Drosophila* to fly off a platform sitting in water is measured (Supplemental Videos). On this island assay, NDUFB10<sup>RNAi</sup> flies took longer to escape compared to controls. We also analyzed the recently-described *Drosophila* whole-body MCU knockout (MCU<sup>1</sup>)<sup>53</sup>. These flies have no ruthenium-red sensitive I<sub>MiCa</sub> (Fig. S6a), and show neither developmental lethality nor flight weakness<sup>53</sup>. When crossed with NDUFB10<sup>RNAi</sup>, however, there was a clear genetic interaction. Double-mutant flies suffered severe developmental lethality and flight muscle weakness (Fig. 6a, b). Notably, these impairments were entirely rescued, reverting NDUFB10<sup>RNAi</sup> flies to near wild-type function, by re-expressing a full-length MCU<sup>53</sup>. To test the importance of the NTD, we created a *Drosophila* ΔNTD-MCU transgene, which targeted mitochondria and was functional in muscle (Fig. S6d-f). This construct, however, entirely failed at rescue, reinforcing the importance of the MCU-Complex I interaction. To confirm the importance of Ca<sup>2+</sup> uptake through the uniporter, we also tested mutant flies that express a flight muscle-restricted pore mutant of MCU (MCU<sup>DQEQ</sup>) that inhibits Ca<sup>2+</sup> transport in a dominant-negative fashion<sup>55</sup>. These *Drosophila* developed in expected numbers and had no flight impairment compared to controls. Here too, a clear genetic interaction was noted between MCU<sup>DQEQ</sup> and NDUFB10<sup>RNAi</sup>, with double-mutant *Drosophila* having substantial developmental lethality and the survivors being impaired in flight (Fig. 6c, d). This genetic interaction was not specific to NDUFB10<sup>RNAi</sup> nor was there a threshold for Complex I impairment necessary, as we saw a similar, milder pattern with NDUF13<sup>RNAi</sup>, which produces a much weaker level of Complex I deficiency (Fig. S6b, c)<sup>29</sup>. Therefore, in *Drosophila* as in *Tfam* KO mice, uniporter activity was necessary to preserve cellular function when Complex I is impaired.

The NTD is critical for the functional, biochemical, and genetic interaction between MCU and Complex I. Moreover, expressing the NTD fragment alone stabilized the uniporter (Fig. 4b), which appears necessary for maintaining homeostasis during Complex I impairment. Reasoning that this strategy may alleviate the phenotype caused by Complex I dysfunction, we generated a construct encoding the isolated *Drosophila* NTD fragment, which also targeted mitochondria (Fig. S6d-f). When expressed in NDUFB10<sup>RNAi</sup> flies, the NTD improved both survival (male flies) and flight, though the rescue was not as complete as expressing full-length MCU (Fig. 6a). Taken together, these results imply that targeting the MCU NTD may be a novel strategy for treating Complex I impairment.

## DISCUSSION

In this report, we identify an essential functional, biochemical, and genetic interaction between Complex I and the uniporter, necessary for survival when Complex I becomes impaired. In deciphering how Complex I dysfunction enhances uniporter levels, we identified CLIPT as a mechanism for MCU protein turnover (Fig. 7), and show that it may be exploited to preserve organismal function during Complex I deficiency, a pathology common to varied diseases.

In deciphering how Complex I dysfunction enhances uniporter levels, we revealed the Complex I interaction is the key determinant for MCU protein turnover, which we term CLIPT. In this process, MCU binding to Complex I leads to uniporter degradation, most likely via oxidative damage from physiological ROS generated in Complex I. Unlike other forms of post-translational MCU regulation, there does not appear to be a specific residue modification driving CLIPT. Rather, as long as MCU and Complex I interact, CLIPT occurs. Aberrant ROS production during Complex I dysfunction may either prevent the MCU-Complex I interaction by modifying the binding site, or lead to Complex I inactivation and disassembly. In either case, enhancement of uniporter levels occurs due to reduced MCU degradation. It remains to be seen if CLIPT controls the turnover of other mitochondrial proteins as well.

Prior studies had hinted at a relationship between the uniporter and Complex I, with biochemical interaction found in several proteomic compendia, and evidence of reduced Complex I levels in *Mcu* KO hearts<sup>39, 40, 56</sup>. We find the MCU-Complex I relationship is evident in *Drosophila*, mouse, and human mitochondria. Notably, such strong evolutionary conservation is reinforced when comparing the species distribution of the uniporter and Complex I, which substantially overlap<sup>57</sup>. Both the uniporter and Complex I are present in animals, plants, and trypanosomes, but absent in yeast.

For the uniporter to undergo CLIPT an intact MCU N-terminal domain is required. The NTD has previously been implicated in binding matrix cations to inactivate the channel<sup>37</sup>, and protein-protein interactions<sup>35, 58, 59</sup>. We found that NTD deletion fully abolished the enhancement in Ca<sup>2+</sup> current seen after Complex I inhibition, whereas overexpression of the NTD by itself made endogenous uniporter channels more degradation-resistant. This ability to enhance endogenous uniporter stability led us to examine the benefits of isolated NTD expression. In proof-of-concept studies, we show that expression of the isolated NTD in models of Complex I impairment can improve muscular function and survival. Targeting this highly conserved relationship may be a potentially novel therapy in disorders that feature Complex I dysfunction.

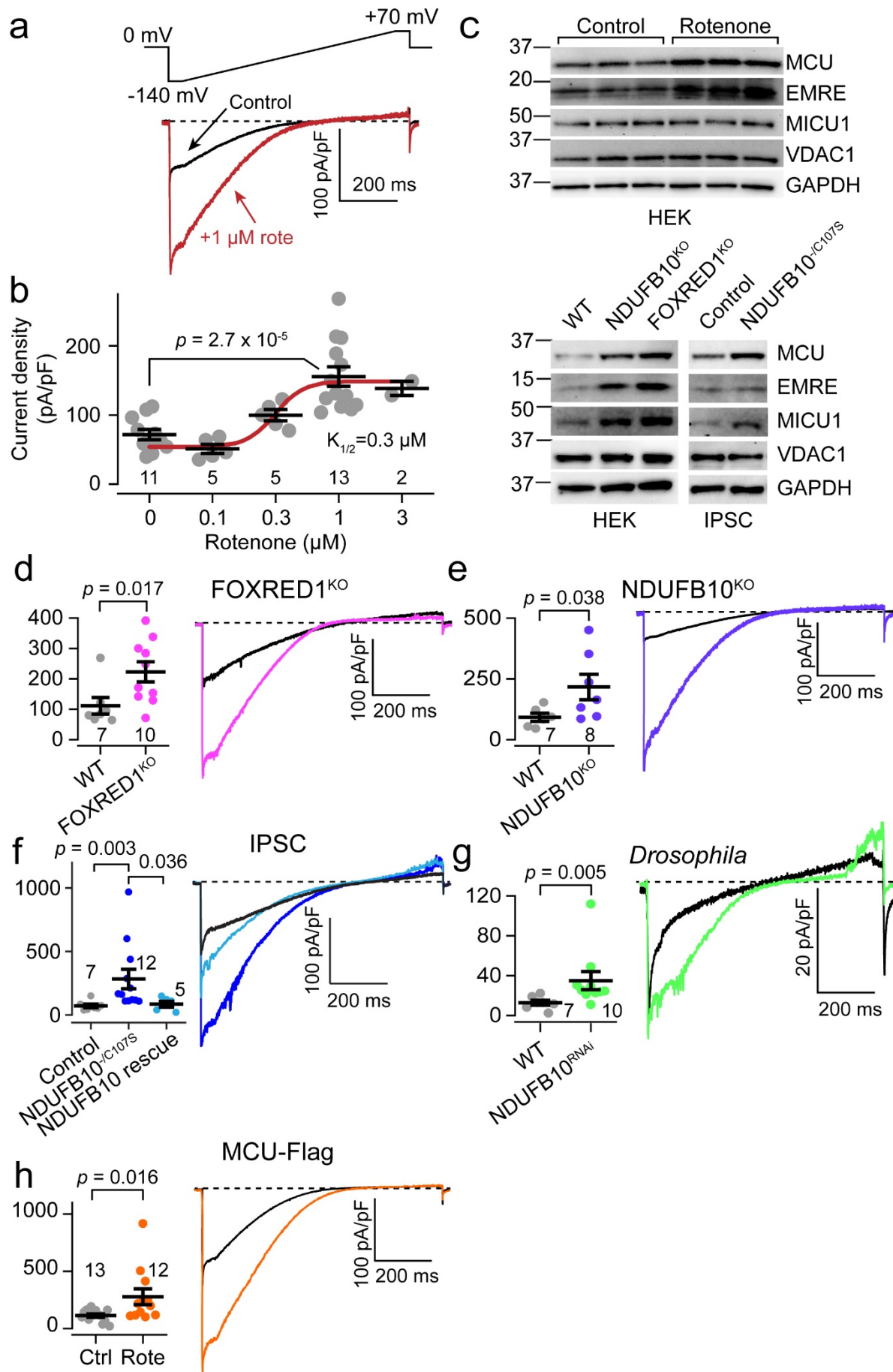


**Figure 1. Complex I dysfunction increases  $I_{\text{MiCa}}$ .** **A.** Top, voltage ramp protocol. Bottom, Exemplar  $I_{\text{MiCa}}$  traces are larger after chronic 1  $\mu\text{M}$  rotenone treatment in HEK293T cells. **B.** Summary rotenone dose-response curve. Black lines represent mean  $\pm$  SEM and N values are listed in the summary graph here and throughout. **C.** Immunoblotting reveals increased uniporter subunit proteins after Complex I impairment in HEK293T, NDUFB10<sup>KO</sup>, FOXRED1<sup>KO</sup>, and patient-derived iPSCs (NDUFB10<sup>-/C107S</sup>) compared to controls. VDAC1 and GAPDH are loading controls. Here and throughout, representative blots from at least 3 replicates are shown. **D-G.** Each panel contains the summary (left) and exemplar (right) for peak inward  $I_{\text{MiCa}}$  in FOXRED1<sup>KO</sup> (**D**), NDUFB10<sup>KO</sup> (**E**), patient-derived iPSCs (**F**), and *Drosophila* NDUFB10<sup>RNAi</sup> (**G**), compared to controls (black). **H.**  $I_{\text{MiCa}}$  is increased in cells expressing MCU-Flag after Complex I impairment.

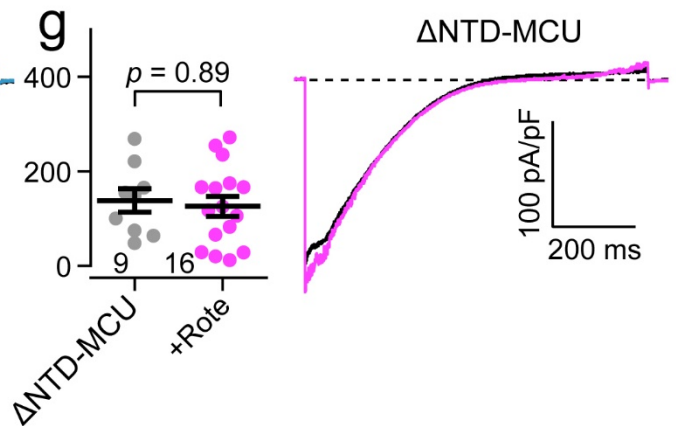
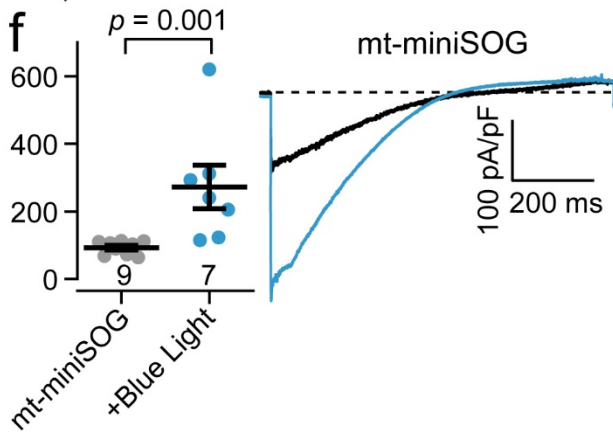
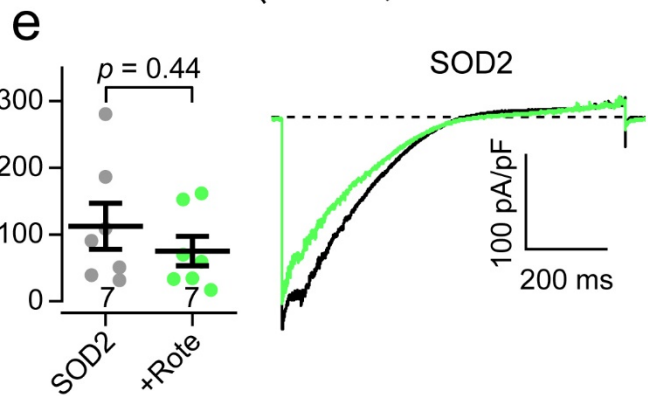
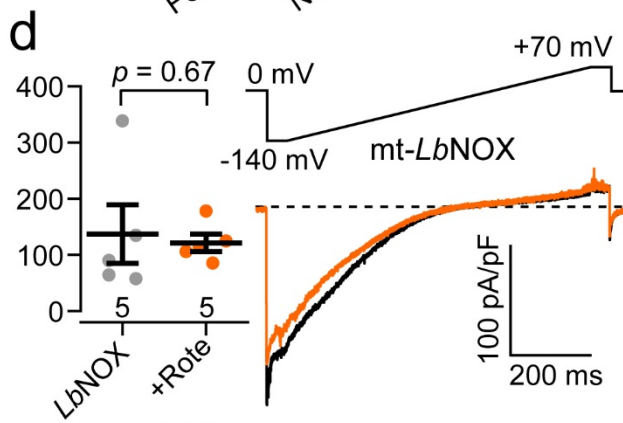
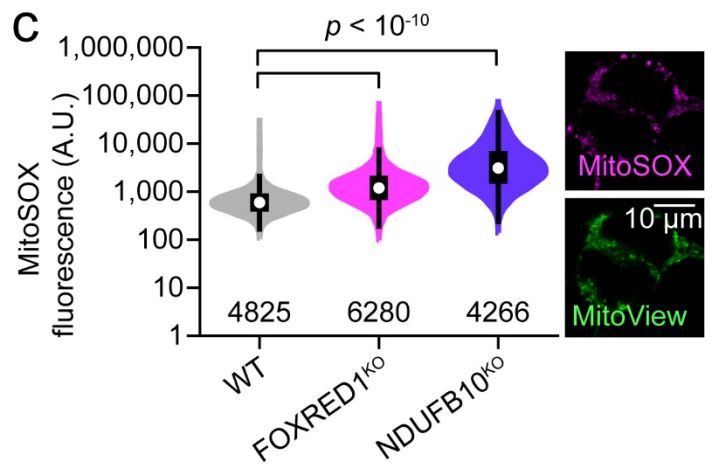
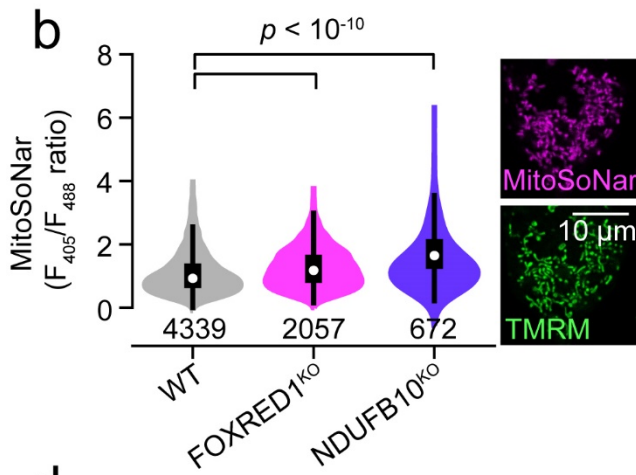
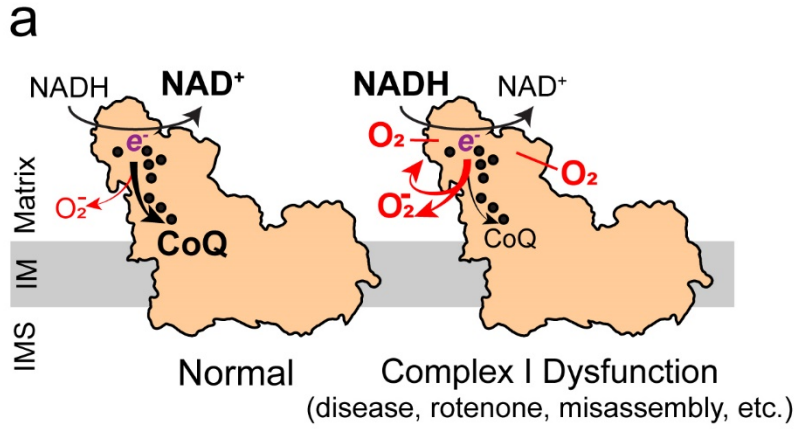


**Figure 2. Reactive oxygen species signal  $I_{\text{Mica}}$  enhancement.** **A.** Complex I cartoon depicting minimal (left) and excessive (right) electron ( $e^-$ ) transfer from NADH to superoxide compared to ubiquinone (CoQ). Excessive  $\text{O}_2^-$  can escape from or self-inactivate Complex I. Black dots, Fe-S clusters. IMS, intermembrane space; IM, inner membrane. **B-C.** Violin plots of MitoSoNar fluorescence ratio (B) and mitochondrial superoxide sensor MitoSOX fluorescence (C) measured via flow cytometry. Insets show mitochondrial targeting of the corresponding sensor. **D-G.** Summary (left) and exemplar (right)  $I_{\text{Mica}}$  in HEK293T cells expressing mito-*LbNOX* (**D**), SOD2 (**E**), mito-miniSOG (**F**), and  $\Delta\text{NTD-MCU}$  (**G**).

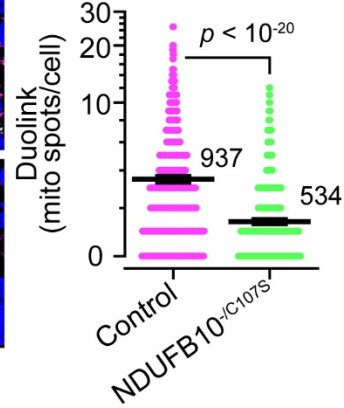
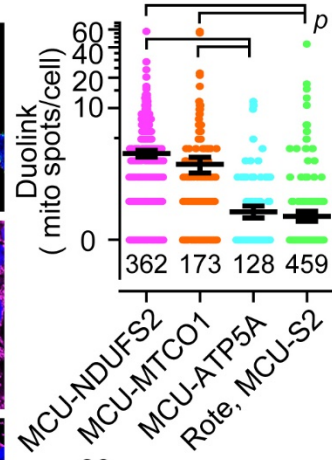
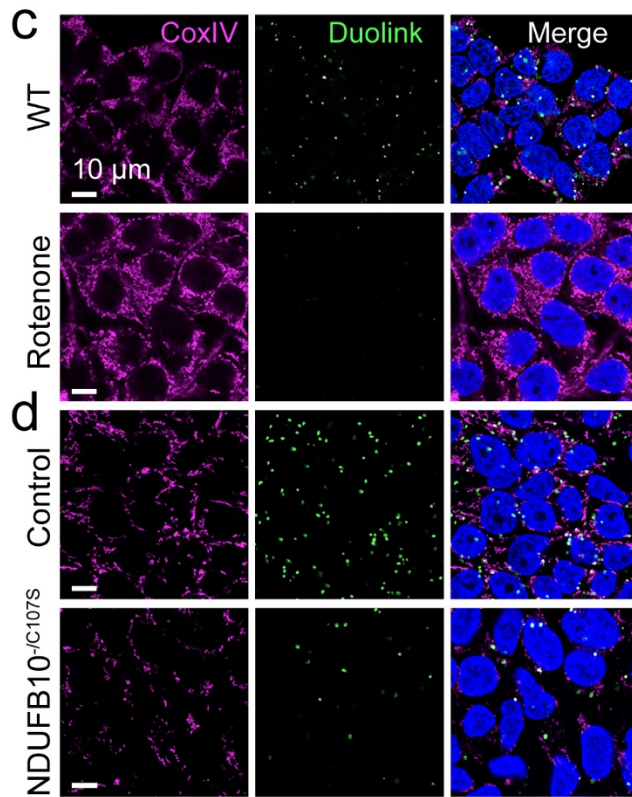
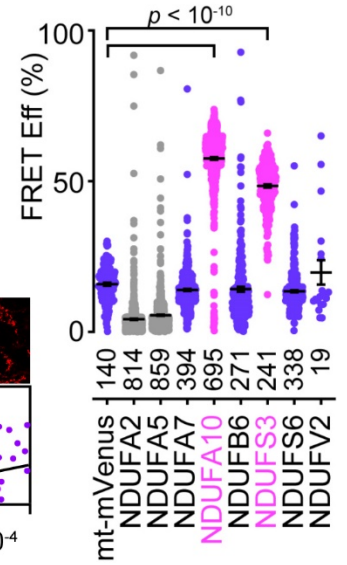
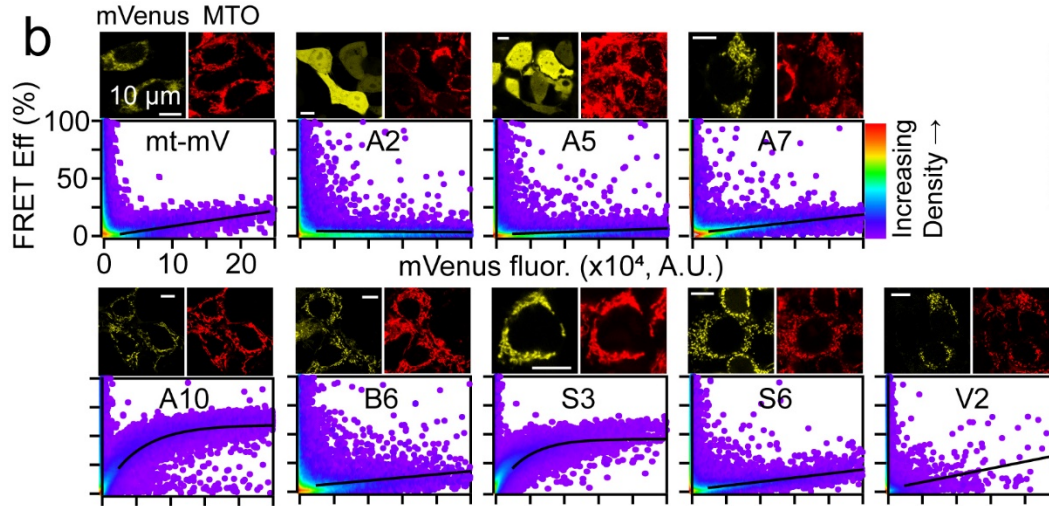
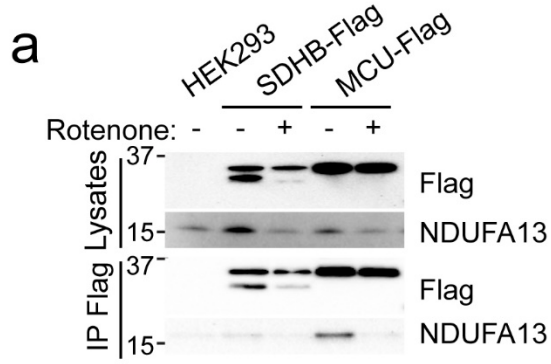


**Figure 3. A direct interaction between MCU and Complex I alters uniporter stability.** **A.** NDUFA13 co-immunoprecipitates with MCU-Flag. **B.** Left, mVenus-tagged Complex I subunits surveyed for FRET with MCU-mCerulean via flow cytometry. Images show mVenus-tagged constructs and MitoTracker Orange (MTO). Density plots display FRET efficiency against mVenus fluorescence for individual cells. Right, FRET summary. **C.** Left, MCU-NDUFS2 Duolink colocalization occurs in mitochondria (CoxIV) and is more prevalent at baseline (WT) than after Complex I inhibition (Rotenone). Right, Duolink summary. Note that 74% of MCU-ATP5A and 85% of Rotenone-treated (MCU-S2) cells had zero Duolink spots, compared to 27% of MCU-NDUFS2 and 37% of MCU-MTCO1 cells. **D.** Left, MCU-NDUFS2 Duolink greater in control than NDUFB10<sup>-/C107S</sup> iPSCs. Right, Summary. 45% of NDUFB10<sup>-/C107S</sup> iPSCs had zero Duolink spots, compared to 19% for control.

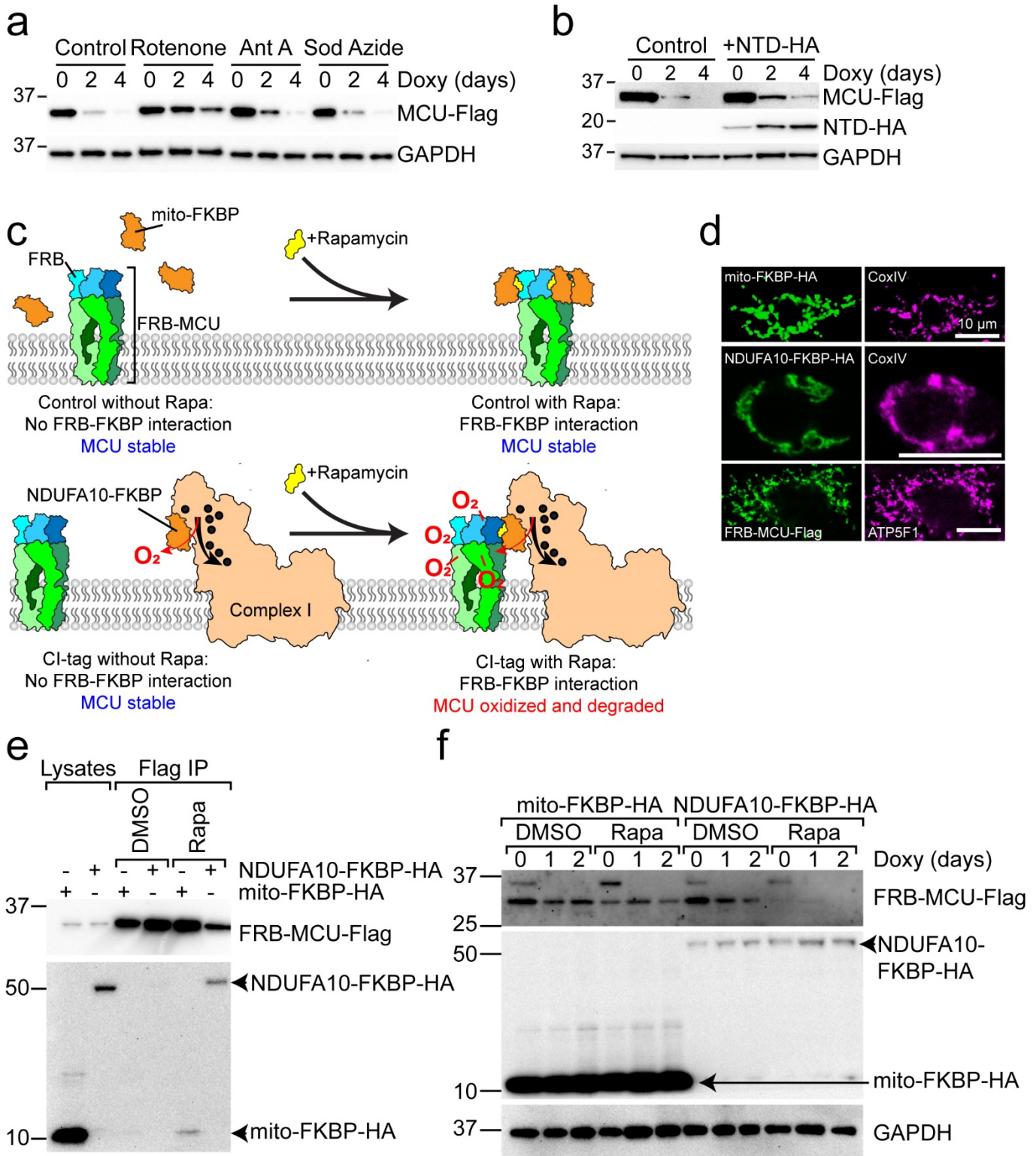


**Figure 4. CLIPT controls MCU degradation.** **A.** Doxycycline (doxy) treatment represses transcription of MCU-Flag. MCU-Flag persists after Complex I inhibition (rotenone) but not Complex III (antimycin A) or IV (sodium azide). **B.** MCU-Flag stabilization induced by NTD peptide. **C.** Design of rapamycin (Rapa)-induced dimerization experiment to test if MCU-Complex I interactions dictate MCU degradation. **D.** Immunocytochemistry reveals co-localization of FRB-MCU, NDUFA10-FKBP, and mito-FKBP with mitochondrial markers CoxIV or ATP5F1. **E.** With replacement of NTD with FRB, MCU only binds FKBP-tagged NDUFA10 in the presence of 100 nM rapamycin. Mito-FKBP-HA is a control. **F.** FRB-MCU is stable in the absence or presence of rapamycin when cells co-express mito-FKBP-HA control, but rapidly degraded when rapamycin induces Complex I-binding in NDUFA10-FKBP-HA expressing cells.

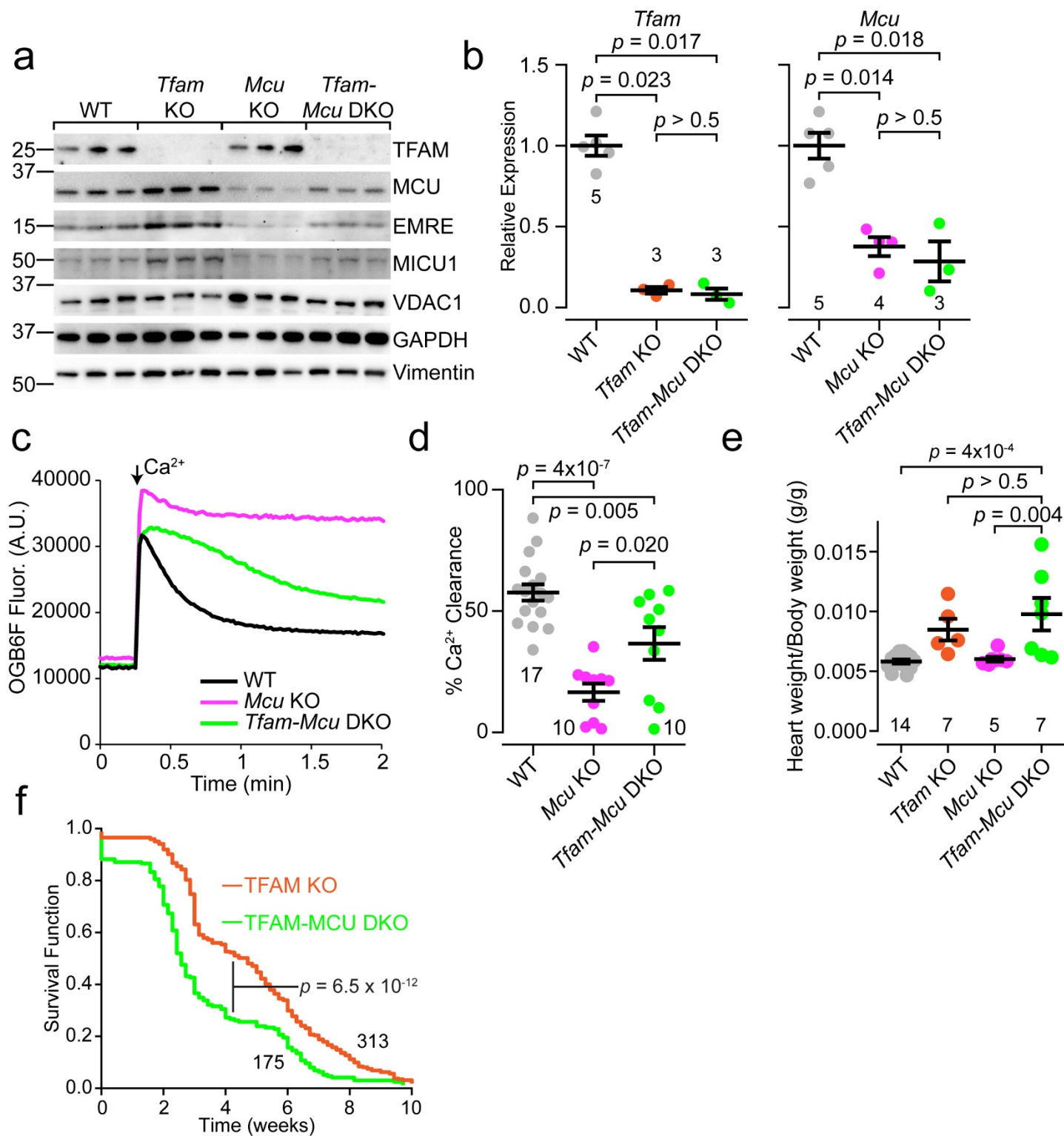


**Figure 5. Diminished MCU degradation is responsible for enhanced uniporter activity in *Tfam* KO hearts, and prolongs survival.** **A.** Immunoblotting for the specified proteins in P10-P14 mouse heart lysates. Samples from 3 mice shown per genotype. **B.** Analysis of *Tfam* and *Mcu* transcripts

in mouse hearts. **C.**  $\text{Ca}^{2+}$  uptake in isolated cardiac mitochondria incubated in Oregon Green BAPTA 6F (OGB6F). Arrow indicates 10  $\mu\text{M}$   $\text{Ca}^{2+}$  pulse. **D.**  $\text{Ca}^{2+}$  clearance measured as the percentage of peak – baseline fluorescence remaining after uptake of the 10  $\mu\text{M}$   $\text{Ca}^{2+}$  pulse. **E.** Heart weight to body weight ratios of P10-P14 mice of the indicated genotypes. **F.** Kaplan-Meier survival analysis of the *Tfam* KO mice compared to *Tfam-Mcu* DKO mice. Comparison via a log rank test.

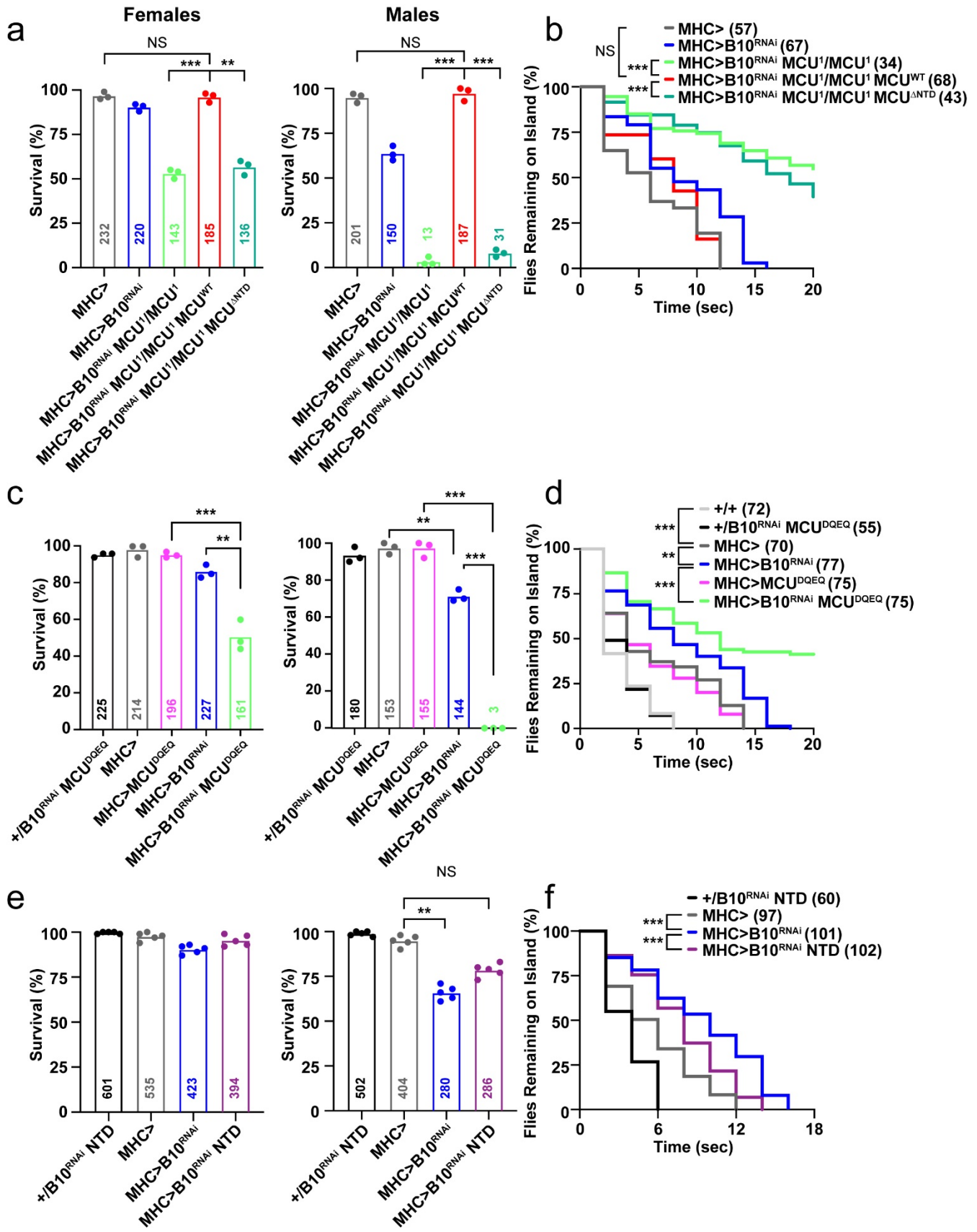


**Figure 6. Genetic interaction between MCU and Complex I in *Drosophila*.** **A, C, E.** *Drosophila* survival for the indicated genotypes and sex. **B, D, F.** Quantification of dwell time in the island assay for indicated genotypes for female flies. **A, B.** The muscle specific *MHC-GAL4* was used to drive expression of *NDUFB10<sup>RNAi</sup>*, *MCU<sup>WT</sup>*, or *MCU<sup>ΔNTD</sup>* in wild-type or *MCU<sup>1</sup>/MCU<sup>1</sup>* mutant flies, as indicated. **C, D.** As in (A, B), except the dominant-negative pore mutant *MCU<sup>DQEQ</sup>* was expressed with *MHC-GAL4*. **E, F.** As in (A, B), except the isolated NTD fragment was expressed with *MHC-GAL4*. \*  $p < 0.05$ , \*\*  $p < 0.01$ , \*\*\*  $p < 0.001$ .

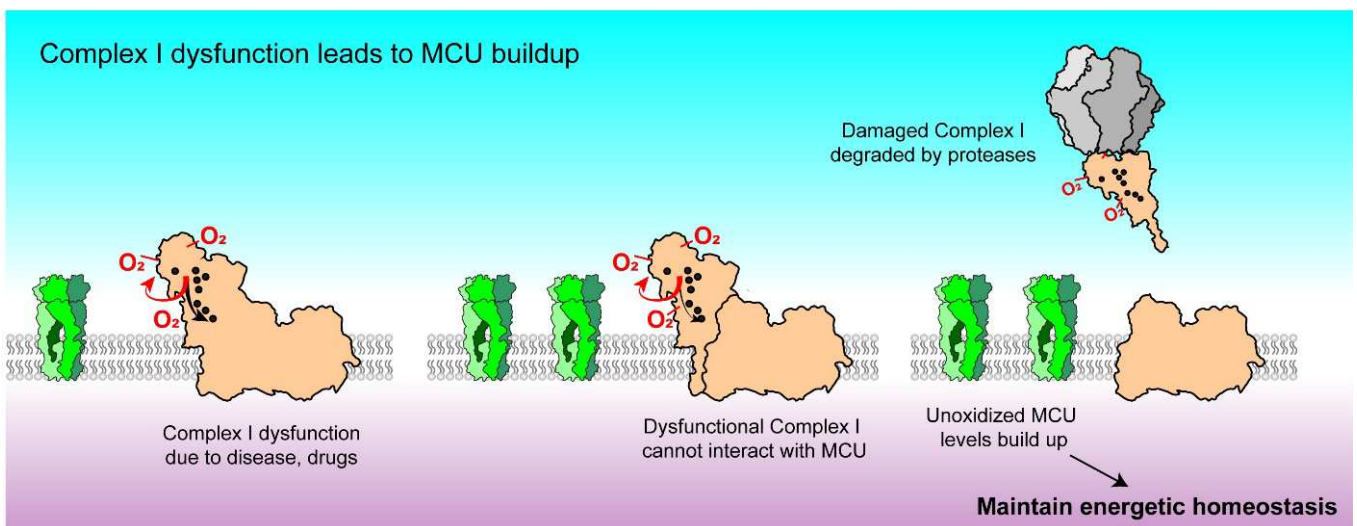
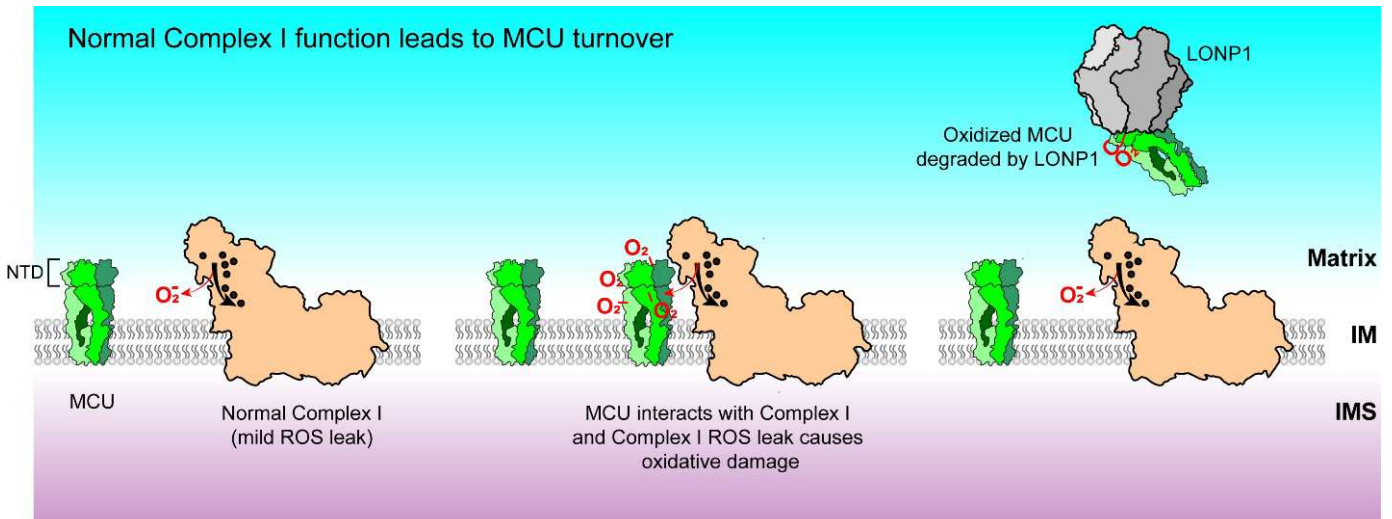


**Figure 7. Complex I ROS controls uniporter turnover.** Top, under physiological conditions, MCU interacts with Complex I and is oxidized by the mild ROS leak produced by Complex I. Such oxidized MCU becomes damaged and degraded by LONP1 or other quality-control proteases, leaving Complex I available to interact with additional channels. Bottom, when Complex I becomes impaired or misassembled, it produces excessive ROS and self-inactivates. Such dysfunctional Complex I can no longer interact with MCU, nor damage it with basal ROS leak, and is cleared by housekeeping proteases CLPP and LONP1. Thus, functional MCU levels build up, and additional  $\text{Ca}^{2+}$  influx through these channels maintains energetic homeostasis.

## METHODS

### Antibodies

ATP5F1 (ab117991, Abcam, 1:1000),  $\beta$ -Actin (ab8224, Abcam, 1:1000), COX IV-Alexa Fluor 488 (4853S, Cell Signaling Tech [CST], 1:200), EMRE (A300-BL19208, Bethyl, 1:1000), FLAG HRP (A8592, Sigma, 1:1000), FLAG magnetic beads (M8823, Sigma), FOXRED1 (sc-377264, Santa Cruz, 1:1000), GAPDH (2118S, CST, 1:1000), HA (3724S, CST, 1:800), HA HRP (12013819001, Sigma, 1:1000), MCU (14997S, CST, WB 1:1000, ICC 1:100, DuoLink 1:200), MICU1 (12524S, CST, 1:1000), MICU1 (HPA037480, Sigma, 1:1000), MTCO1 (ab14705, Abcam, 1:100), NDUFA13 (ab110240, Abcam, 1:1000), NDUFB10 (ab196019, Abcam, 1:1000), NDUFS2 (ab110249, Abcam, WB 1:1000, ICC 1:100, DuoLink 1:200), NDUFS3 (ab177471, ICC 1:200), NDUFS4 (ab137064, WB 1:1000), Oct4 (ab19857, Abcam, 1:200), ROMO1 (TA505580, Origene, 1:1000), Sox2 (5024, CST, 1:200), ZO-1 (33-9100, ThermoFisher, 1:200), VDAC1 (ab14734, Abcam, 1:1000), Vimentin (ab92547, Abcam, 1:1000).

### Plasmids for stable expression, transient transfection, and short hairpin RNA

Newly-derived plasmids were created using the NEB HiFi DNA Assembly Cloning Kit (Ipswich, MA), and will be deposited at Addgene. Plasmids were verified by Sanger sequencing.

pUC57-mito-*LbNOX* (Addgene #74448), pLYS5-SDHB-Flag (Addgene #50055), pLYS1-MCU-Flag, pLYS1- $\Delta$ NTD-MCU-Flag (removing amino acids 58-186), and pLYS1-Cys-Free-MCU-Flag were gifts from Vamsi Mootha<sup>23, 25, 60, 61</sup>. pGP-CMV-GCaMP6m was a gift from Douglas Kim & GENIE Project (Addgene #40754). MiniSOG-Mito-7 (Addgene #57773) was a gift from Michael Davidson<sup>33</sup>. pCW57.1-MAT2A (Addgene #100521) was a gift from David Sabatini<sup>45</sup>. CFP-FKBP (Addgene #20160) and YFP-FRB (Addgene #20148) were gifts from Tobias Meyer<sup>62</sup>. pUASg.attB was a gift from Johannes Bischof and Konrad Basler. SoNar was a gift from Yi Yang<sup>32</sup>.

Mito-*LbNOX* was expanded from pUC57-mitoLbNOX and cloned into pLenti-CMV-puro for lentiviral generation. GCaMP6m was cloned into pLenti-CMV-puro with an N-terminal Cox8 mitochondrial targeting sequence and a C-terminal mCherry tag. Human SOD2 was expanded from a HEK293T cDNA library and cloned into pLenti-CMV-puro with a C-terminal HA tag. The mitochondrial targeting sequence from ABCB10 (aa 1-193) was expanded from a HEK293T cDNA library and cloned in-frame upstream of SoNar to create mitochondrially-targeted MitoSoNar. MCU-Flag was shuttled from pLYS1-MCU-Flag into pCW57.1-MAT2A to create pCW57.1-MCU-Flag. The MCU NTD (aa 1-185) was expanded from pLYS1-MCU and cloned into pLenti with an HA-tag at its C-terminus. FRB-MCU was generated by incorporating the FRB fragment immediately downstream of the mitochondrial targeting sequence within  $\Delta$ NTD-MCU-Flag, and placing this in the pCW57.1-MAT2A plasmid. For mito-FKBP, the FKBP fragment was placed between a 4-fold repeat of the COX8A mitochondrially targeting sequence and an HA tag in pLenti-CMV-puro. NDUFA10-FKBP was created similarly, except the full NDUFA10 sequence was used instead of the mitochondrial targeting sequence. *Drosophila* MCU lacking amino acids 56-182 was cloned (UniProt Q8IQ70), along with a C-terminal HA tag, from pAC5.1<sup>59</sup> into pUASg.attB to create  $\Delta$ NTD-MCU-pUASg.attB. A similar strategy was used to incorporate the *Drosophila* MCU NTD fragment (amino acids 1-182), creating NTD-pUASg.attB.

For FRET experiments, mitochondria-targeted mVenus (mt-mVenus) and mCerulean (mt-mCerulean) were created by adding four copies of the human COX8 mitochondrial targeting sequence to the N-terminal of mVenus in the pLenti-CMV-puro backbone. The sequence for MCU was expanded from pLYS1-MCU-Flag and cloned into the mCerulean-pLenti vector in place of the

mitochondrial targeting sequence. Sequences for NDUFA2, NDUFA5, NDUFA7, NDUFA10, NDUFS3, NDUFS6, NDUFB6, and NDUFV2 were expanded from a HEK293T cDNA library via polymerase chain reaction and cloned N-terminal to mVenus in a pEGFP vector. For FRET calibration, we also cloned mitochondrially-targeted mVenus-mCerulean dimers separated by linkers of 5, 43, and 236 amino acids into pLenti-CMV-puro to create mito-C5V, mito-C43V, and mito-CTV.

Short hairpin RNA lentiviral constructs were obtained from The RNAi Consortium (Sigma). TRC IDs for shRNA plasmids are TRCN0000412514 (AFG3L2), TRCN0000046859 (CLPP), TRCN0000310154 (LONP1), TRCN0000046793 (LONP1), TRCN0000063825 (SPG7). The control was shGFP (SHC005).

### **Cell culture and generation of stable lines**

HEK293T cells were grown in Dulbecco's Modified Eagle Medium (DMEM) (ThermoFisher) with 10% fetal bovine serum, penicillin (100 I.U./ml), streptomycin (100 µg/ml). Cells that had genetic or pharmacological inhibition of Complex I (and their respective controls) were also supplemented with 0.4 mM uridine and 2 mM pyruvate. For pharmacological inhibition, media was supplemented with 0.1-3 µM rotenone (Complex I), 1 µM Antimycin A (Complex III), or 200 µM sodium azide (Complex IV), as indicated, 48-72 hours prior to use. For generation of stable lines, cells were transduced with lentivirus and selected with 1.5 µg/mL puromycin or 10 µg/mL blasticidin.

NDUB10 and NDUFS4 knockout HEK293T cells were a kind gift of Michael Ryan<sup>24</sup>.

HEK293T genetic fingerprinting validation is via short tandem repeat analysis, performed at the University of Utah DNA Sequencing Core.

### **FOXRED1 knockout line generation**

HEK293T cells were electroporated (Neon Transfection System, Thermo Fisher) with Alt-R Sp HiFi Cas9 nuclease v3, tracrRNA, and FOXRED1 crRNA (Hs.Cas9.FOXRED1.1.AA and Hs.Cas9.FOXRED1.1.AC), all from Integrated DNA Technologies (Coralville, IA) per the manufacturer's instructions. Single clones were expanded and plated in both DMEM + 10% FBS media containing 0.4 mM uridine, 2 mM pyruvate and either 25 mM glucose or 10 mM galactose. Clones that failed to grow in galactose had genomic DNA Sanger sequenced for evidence of editing, and clones were subject to Western blot to confirm FOXRED1 deletion, and one of these that appeared to grow well was further studied.

### **Patient-derived induced pluripotent stem cells**

Fibroblasts obtained post-mortem from an infant with NDUFB10 deficiency (NDUFB10<sup>-/C107S</sup>)<sup>28</sup> were reprogrammed into iPSCs using CytoTune-iPS Sendai Reprogramming vector (A16517, ThermoFisher), and cultured in Essential 8 stem cell media (A1517001, ThermoFisher) supplemented with 2 mM pyruvate, 0.4 mM uridine, and 1 mM N-acetylcysteine. At around Day 20 post-transduction, newly formed iPSC colonies were transferred to new plates and expanded for another month. For quality control of iPSCs we performed four standard assays to determine (1) pluripotent status, (2) genetic fingerprinting, (3) karyotype and (4) absence of bacterial or mycoplasma contamination. Pluripotent status was determined by immunofluorescence against Oct4, Sox2, and ZO-1, and counterstained with Hoechst dye prior to imaging on a fluorescent EVOS Cell Imaging System (ThermoFisher). iPSC genetic fingerprinting is via short tandem repeat analysis. Molecular karyotyping of genomic DNA is via an nCounter Human Karyotype Assay

(Nanostring Technologies Inc.). Contamination testing is via an e-Myco PLUS Mycoplasma PCR Detection Kit (iNtRON Biotechnology) and an PCR Bacteria Test Kit (PromoCell GmbH).

Control and *NDUFB10*<sup>-/-C107S</sup> iPSCs were cultured in 6-well culture plates coated with vitronectin (A14700, ThermoFisher) in StemFlex medium (A3349401, ThermoFisher) medium containing 10  $\mu$ M Y-27632 ROCK inhibitor (S1049, SelleckChem, Houston, TX), 2 mM pyruvate, and 0.4 mM uridine, changed daily.

### Mouse strains and survival

All animal procedures have been reviewed and approved by the Institutional Animal Care and Use Committee at the University of Utah and Boston Children's Hospital. *Tfam*<sup>loxP/loxP</sup> mice were developed by Nils-Göran Larsson<sup>13</sup> and obtained from Ronald Kahn<sup>63</sup>. *Mcu*<sup>loxP/loxP</sup> mice were obtained from John Elrod<sup>18</sup>. *Myh6-Cre* transgenic mice were obtained from the Jackson Laboratory (Bar Harbor, ME, stock # 011038)<sup>64</sup>. Animals were kept on a C57BL/6J background. Animals were housed under standard conditions and allowed free access to food and water. Animals used for experiments were 10-14 days old. Heart and body weights were recorded at time of euthanasia. Survival analysis was performed in OriginPro 9 (OriginLab). A Kaplan-Meier curve was constructed, censoring animals used for experiments. Statistical comparison was via a log-rank test.

### Fly Stocks and maintenance

Fly rearing was done on standard cornmeal/yeast/molasses food prepared in a central kitchen at the University of Utah. The following *Drosophila melanogaster* strains were used: *w Berlin* control strain (obtained from Adrian Rothenfluh, University of Texas Southwestern Medical Center, Dallas, TX); *w*; *MHC-GAL4/TM6C,Sb*, *w*<sup>1118</sup>; *da-GAL4*, *yw*; *UAS-NDUFB10*<sup>RNAi</sup>, and *yw*; *UAS-NDUFA13*<sup>RNAi</sup> (obtained from Edward Owusu-Ansah, Columbia University; Bloomington Drosophila Stock Center numbers 55133, 29592, and 43279)<sup>29</sup>; *w*; *UAS-MCU*<sup>D206Q,E263Q</sup> (obtained from Ronald Davis, The Scripps Research Institute Florida; Jupiter, FL)<sup>55</sup>; *w*; *MCU*<sup>1</sup>/*MCU*<sup>1</sup> and *w*; *UAS-MCU*<sup>WT</sup> (obtained from Alex Whitworth, University of Cambridge, Cambridge, UK)<sup>53</sup>. PhiC31 integrase-mediated transgenic flies were generated by BestGene (Chino Hills, CA) from NTD-pUASg.attB. Integration site was at attP40, as with *UAS-MCU*<sup>WT</sup>. Genomic PCR confirmation of insertion and subsequent balancing were performed by BestGene. Flies were reared at 25 °C in a 12:12 light/dark cycle. Fly genotypes are listed in Supplemental Table 1.

### Mitochondrial and mitoplast isolation

Mitochondria were isolated from cultured cells or mouse hearts by differential centrifugation, and mitoplasts prepared as previously described<sup>12, 15</sup>. For *Drosophila* mitochondrial isolation, lines were raised at 20°C. Adult flies >3 days of age after eclosion were used. Mitochondria were prepared from thoraces (devoid of legs and wings) of >50 flies. Thoraces were homogenized with a Potter-Elvehjem grinder set to 250 rpm, and the remainder of the protocol was as previously described<sup>15</sup>.

### Electrophysiology

Whole-mitoplast electrophysiology was performed as described previously<sup>15</sup>. For *Drosophila*, we used MHC-Gal4 driven expression to measure changes in flight muscle *I*<sub>MiCa</sub>. To confirm with electrophysiology that transgenes were expressing, we used the global Da-Gal4 driver for  $\Delta$ NTD-*MCU* *I*<sub>MiCa</sub> in *MCU*<sup>1</sup> flies, and isolated MCU NTD in wild-type flies. Borosilicate glass pipettes with

a resistance of 15-20 M $\Omega$  were used. Whole-mitoplasts currents were acquired at 5 kHz and filtered at 1 kHz using an Axopatch 200B amplifier (Molecular Devices, San Jose, CA). Mitoplasts had a capacitance 0.2-3.7 pF. Pipette solution was composed of (mM): Na-Gluconate 150, HEPES 10, EDTA 1, EGTA 1, pH 7.2, brought up to 320-340 mOsm with D-Mannitol. Bath solution for inner membrane anion channel (mM): 150 KCl, 10 HEPES, 1 EGTA. Bath solution for mitochondrial calcium uniporter (mM): Na-Gluconate 150, HEPES 10, 5 CaCl<sub>2</sub>, pH 7.2. A ~12 mV junction potential was cancelled on switching between solutions. Ruthenium red (1  $\mu$ M) was added to block uniporter-specific currents. For display purposes, capacitance transients caused by changing levels of solutions in the bath have been removed and the Simplify filter from Adobe Illustrator has been used to reduce the number of points, without altering the shape of the traces. Analysis was performed using pClamp v10 (Molecular Devices), Excel (Microsoft), and OriginPro 9. For statistical comparisons, we used two-sided Mann-Whitney U tests, except for the rotenone concentration-response curve, for which we used ANOVA with post-hoc Bonferroni-corrected means comparisons, and the IPSC KO and rescue experiment, for which we used a Kruskal-Wallis test to establish overall *p* value, followed by Bonferroni-corrected Dunn's test for pairwise comparisons.

### **Quantitative reverse transcription-polymerase chain reaction (qPCR) expression analysis**

Quantitative PCR from IPSC, HEK293T cells, and mouse hearts was performed as described previously, using Power SYBR Green PCR Master Mix (ThermoFisher)<sup>12</sup>. Quantification of gene expression was performed on a 96-well BioRad CFX Connect Real-Time PCR Detection System (BioRad, CA, USA). Analysis was performed by using the  $2^{-\Delta\Delta C_t}$  method. Primers were obtained via NCBI Primer-BLAST, Primerbank, or prior reports<sup>65,66</sup>.

### **Western blots**

Cells or tissue were lysed in RIPA buffer containing Halt protease and phosphatase inhibitor cocktail (78440, ThermoFisher). After lysate clarification, protein concentration was determined by BCA assay (23227, Thermo Fisher). 5-20  $\mu$ g of protein from cell lysates were loaded on polyacrylamide gels and immunoblotted as described previously<sup>59</sup>.

### **Blue light assay for miniSOG**

HEK293T cells expressing mito-miniSOG at >70% confluence were exposed to blue light from an LED array for 10 min at RT. Longer periods of blue light exposure would often lead to substantial cell death. Mitoplast isolation as described above was performed 48-72 hours later. Cells with the same construct without exposure to blue light were used as control.

### **Flow cytometric measurements**

Data was collected at the Flow Cytometry Core Facility at the University of Utah. For mitochondrial ROS measurements, cells were incubated with 5  $\mu$ M MitoSOX (M36008, ThermoFisher) at 37°C for 15-30 minutes. For mitochondrial NADH/NAD<sup>+</sup> measurement, cells were transfected 24-48 hours prior to analysis with the MitoSoNar construct. Cells were analyzed with a BD FACSCanto Analyzer running FACSDiva 6 software (both BD Biosciences, San Jose, CA). For mitochondrial Ca<sup>2+</sup>, mito-GCaMP6m was measured using 488 nm excitation laser and 530/30 nm emission filters and mCherry was measured using a 561 nm laser and 585/15 nm emission filter. For MitoSOX, we used a 488 nm excitation laser and 585/15 nm emission filter. For MitoSoNar, we used the ratio of 525/50 nm emissions when excited by either 405 nm or 488 nm laser lines after background correction in untransfected cells. For analysis, live, single cells were selected using forward and side-scatter parameters. Analysis was performed on FlowJo (v10.6, BD Life

Sciences, Ashland, OR) and OriginPro 9. Statistical test was via ANOVA with post-hoc Bonferroni-corrected means comparisons.

### **LbNOX Cell proliferation assays**

One hundred thousand HEK293T WT, MCU KO, mito-LbNOX, or MCU KO mito-LbNox cells were seeded in a 6-well dish containing 2 mL DMEM (ThermoFisher) with 10% FBS (Life Technologies), penicillin (100 I.U./ml), streptomycin (100 µg/ml), 1x Glutamax (ThermoFisher), 0.4 mM uridine (Fisher Scientific), and either 0 or 500nM mM piericidin (Cayman Chemical). Medium was exchanged every twenty-four hours. After 2, 4, and 7 days, cells in each well were trypsinized and counted using a Z1 Coulter Counter (Beckman Coulter).

### **Confocal imaging and immunocytochemistry**

To determine targeting of mCerulean- and mVenus-tagged constructs we used live cell confocal imaging. Cells were washed with phosphate buffered saline and incubated with 100 nM MitoTracker Orange CMTMRos (M7510, ThermoFisher) or MitoView Green (70054, Biotium, Fremont, CA).

For immunocytochemistry, cells were grown on poly-L-lysine-coated glass coverslips. After phosphate buffered saline washes, cells were fixed in 10% neutral buffered formalin (VWR), permeabilized with 1% Triton X-100, and blocked with fetal goat serum. Primary antibodies were incubated at the indicated dilutions, and when needed secondary antibodies were goat anti-mouse Alexa Fluor 555 or goat anti-rabbit Alexa Fluor 488.

For *Drosophila* imaging, flies were embedded in Tissue-Tex O.C.T. Compound (Sakura), sliced to 7 µm thickness and mounted on glass coverslips. The sections were fixed using Formalin (Fisher Healthcare), permeabilized using 0.5% Triton X-100, and blocked using goat serum. Staining with primary antibodies occurred overnight in the presence of *Drosophila* larvae homogenate in 0.2% Triton X-100. Secondary antibodies were goat anti-mouse Alexa Fluor 555 or goat anti-rabbit Alexa Fluor 488.

Image acquisition was at room temperature. Imaging was performed on a Leica TCS SPE confocal microscope (Buffalo Grove, IL) using Leica Application Suite X v3.5 software. Acquisition was for 1024 x 1024 pixels at an 8-bit depth. Images have been enhanced for contrast uniformly, without alteration of gamma, and pseudocolored from grayscale.

### **Affinity Purification and Co-Immunoprecipitation**

HEK293T cells stably expressing MCU-Flag were grown to confluency, while wild-type cells and cells stably expressing SDHB-Flag served as controls. After washing in phosphate-buffered saline, cells were lysed in 1% digitonin, 50 mM Tris, 150 mM NaCl and Halt protease and phosphatase inhibitors. Lysates were centrifuged at 4 °C for 10 minutes at 16000g. 200-500 µg of cleared lysates were incubated with 10 µl of FLAG antibody conjugated beads overnight at 4 °C. For co-immunoprecipitation studies, after extensive washing, the beads were heated to 80°C in 50 µl of sample loading buffer and then used for Western blotting as described above.

For proteomic analysis, cells were processed as above but eluted in 2% SDS in mass spectrometry-grade water. We analyzed six independent MCU-Flag samples and four control non-transduced samples.

### **Liquid chromatography-tandem mass spectrometry**

Sample preparation for mass spectrometry was performed as described previously<sup>67, 68</sup>. Briefly, samples were diluted with UA buffer, reduced, alkylated and proteins were digested with trypsin overnight at 37°C, then acidified using 1% formic acid. Peptides were analyzed with an Orbitrap Velos Pro mass spectrometer (Thermo) interfaced with an EZ nLC-1000 UPLC and outfitted with a PicoFrit reversed phase column (15 cm x 75 µm inner diameter, 3 µm particle size, 120 Å pore diameter, New Objective). Spectra were acquired in a data-dependent mode with dynamic exclusion. MS1 spectra were acquired at a resolution of 30,000 and the top 20 peaks were fragmented using CID fragmentation and analyzed in ion trap. The top twenty MS1 peaks were analyzed at a resolution of 30,000. Samples were run in duplicate.

The resulting spectra were analyzed using MaxQuant 1.6.0.16 against the UniprotKB human database. Database search engine parameters were as follows: trypsin digestion, two missed cleavages, precursor mass tolerance of 20 ppm, fragment mass tolerance of 0.5 Da, and dynamic acetyl (Protein N-term), and oxidation (M). The false discovery rate (FDR) was 1% and modified peptides had a minimum Andromeda score of 40. The proteins identified were further filtered to only include those identified in at least 50% of all FLAG pull downs as confident interactors. For relative quantification, peptide abundance was log2 transformed and missing values were imputed with Perseus 1.6.5.0. Normalized log2 intensities of peptides were used in statistical comparisons of groups: Student's two sample t-test was used for comparisons between the two sample groups and volcano plots were generated with an FDR of 0.1. Statistical analyses were performed in Perseus 1.6.5.0.

### Flow cytometric Förster resonance energy transfer

Data was collected at the Flow Cytometry Core Facility at the University of Utah. We followed the protocol described previously to quantify FRET using flow cytometry<sup>43</sup>. Cells in 6-well dishes were transfected with 5 µg plasmid DNA using Lipofectamine 2000 (Thermo) 1-3 days prior to analysis. On the day of cytometry, cells were incubated with 100 µM cycloheximide for ~2 hours prior to analysis, to prevent artifacts from incomplete protein synthesis<sup>43</sup>. Flow cytometry was performed on a BD FACSCanto Analyzer. Signals were recorded using (1) 408 nm laser excitation and 450/50 nm emission (mCerulean), (2) 408 nm excitation and 525/50 emission (FRET), and (3) 488 nm excitation and 530/30 nm emission (mVenus). In all cases, we subset populations for live fractions of single cells using forward and side-scatter parameters. We obtained signals from untransfected cells for background correction. Background-corrected signals are designated  $S_{Ven}$ ,  $S_{Cer}$ , and  $S_{FRET}$  for the excitation/emission pairs 488/530, 408/450, and 408/525, respectively. Signals from mt-mVenus transfected alone were used to calculate the cross-talk ratio between  $S_{Ven}$  and  $S_{FRET}$  ( $R_{A1}$ ), while signals from mt-mCerulean transfected alone were used to calculate the cross-talk ratios between  $S_{Cer}$  and  $S_{FRET}$  ( $R_{D1}$ ) and between  $S_{Cer}$  and  $S_{Ven}$  ( $R_{D2}$ ). These ratios were then used to correct for cross-talk signals within each analyzed cell co-transfected with MCU-mCerulean and either mt-mVenus or each of the mVenus-tagged NDUF constructs (NDUFA2, NDUFA5, NDUFA7, NDUFA10, NDUFS3, NDUFS6, NDUFB6, and NDUFV2). The correction calculations are:

$$Cer_{direct} = R_{D1} \times S_{Cer} \quad (1)$$

$$Ven_{direct} = R_{A1}(S_{Ven} - R_{D2} \times S_{Cer}) \quad (2)$$

$$Ven_{FRET} = S_{FRET} - Cer_{direct} - Ven_{direct} \quad (3)$$

where (3) is the FRET signal corrected for cross-talk from fluorescence due directly to mVenus and mCerulean, calculated using the prior ratios and equations (1)-(2). Next, to calibrate the FRET

signal, we make use of the mitochondria-targeted mVenus-mCerulean dimers with varying linkers. Because of the one-to-one relationship between FRET donor (mCerulean) and acceptor (mVenus) in these constructs, the following equation holds true

$$\frac{Ven_{FRET}}{Cer_{direct}} = \frac{g_{Cer}}{g_{Ven}} \times \frac{Ven_{direct}}{Cer_{direct}} - \frac{f_{Ven}}{f_{Cer}} \quad (4)$$

where instrument- and fluorophore-related constants for excitation and emission are captured in the  $g$  and  $f$  terms, respectively. Because this is a linear equation, by plotting  $\frac{Ven_{FRET}}{Cer_{direct}}$  against  $\frac{Ven_{direct}}{Cer_{direct}}$  for the three mVenus-mCerulean pairs we can obtain the intercept  $\frac{f_{Ven}}{f_{Cer}}$  from the best-fit regression line. Our value of 1.62 was in close agreement with the 1.65 value obtained in the prior publication, even with different instruments and mitochondria-targeted fluorophores. Finally, we calculated donor FRET efficiency for each cell by using the equation

$$\langle E \rangle_{Cer} = \frac{Ven_{FRET}}{Ven_{FRET} + \frac{f_{Ven}}{f_{Cer}} \times Cer_{direct}} \quad (5)$$

and plotting against the mVenus fluorescence of that cell.

Analysis was carried out in FlowJo and Excel. Data was then exported to OriginPro 9 for display as density plots. For display, we fit a straight line to those constructs that demonstrated no FRET or concentration-dependent spurious FRET, or an exponential of the form  $y = a(1 - e^{-bx})$  for the constructs that demonstrated strong FRET. For the summary graph in Fig. 3b, we used the FRET efficiencies in the fluorescence window of 150,000-200,000 for mVenus expression. Statistical comparisons were in OriginPro 9 via ANOVA with post-hoc Bonferroni-corrected means comparisons.

### Duolink proximity ligation assay

Duolink proximity ligation (DUO92102, Sigma) assays were performed per the manufacturer's protocol. We used monoclonal mouse anti-NDUFS2, and monoclonal rabbit anti-MCU, both of which have been knockout validated. Mitochondrial counterstain was with anti-COX IV-Alexa Fluor 488. Cells were imaged on a confocal microscope as described above. Areas for imaging were selected based on uniform distribution of DAPI-stained nuclei with about 20-50 cells per field. Separate images were taken of each field for DAPI (nuclei, 405 nm laser), COX IV-Alexa Fluor 488 (mitochondria, 488 nm laser), and Duolink spots (561 laser). Analysis was performed on CellProfiler (v3.1)<sup>69</sup>. After median filtering DAPI-stained nuclei, the ExpandObjects module was used to dilate these until touching adjacent objects to define cell borders. Mitochondrial objects were identified in median-filtered COX IV stained images, and Duolink spots were identified in the Duolink images. To detect Duolink spots corresponding to mitochondria the RelateObjects module was used, and any non-mitochondrial Duolink spots filtered out. Spots were assigned to the cell object they were in to generate an estimate of spots per cell. Results were analyzed in Excel and OriginPro 9 using ANOVA with post-hoc Bonferroni-corrected means comparisons. For display purposes only, the size and contrast of the Duolink spots in the manuscript figures have been increased uniformly to allow visualization with the small figure size.

### Doxycycline repression for determining MCU stability

Stable lines expressing pCW57.1-MCU-Flag (derived from pCW57.1-MAT2A<sup>45</sup>) allowed repression of MCU transcription by doxycycline. The cells were grown using media supplemented with 3%

fetal bovine serum, to minimize cell division. Day 0 cells were collected immediately prior to doxycycline addition, and the remaining cells were incubated with 1 µg/mL doxycycline for the indicated number of days. For Complex I inhibition, cells were incubated in 1 µM rotenone for 48 hours prior to doxycycline addition.

### **Rapamycin-induced dimerization**

Stable cell lines were created using lentiviral transduction, expressing (1) FRB-MCU-Flag and mito-FKBP-HA, or (2) FRB-MCU-Flag and NDUFA10-FKBP-HA. Co-immunoprecipitation was performed as described above, except lysates were incubated with either DMSO or 100 nM rapamycin during affinity purification overnight at 4°C. For stability studies, cultured cells were incubated with DMSO or 100 nM rapamycin for one day prior to adding 1 µg/mL doxycycline, and cells were collected and processed for Western blotting at the indicated timepoints as described above.

### **Mitochondrial Ca<sup>2+</sup> Imaging**

Imaging was performed in 96-well plates on a Cytation 5 microplate reader (Biotek, Winooski, VT). For mice, 100 µg of cardiac mitochondria were used per trial. For HEK293T, 10<sup>5</sup> cells were permeabilized with 0.005% digitonin and used per trial. Samples were incubated in 100 µL of solution containing (in mM): 125 KCL, 20 HEPES, 5 K<sub>2</sub>HPO<sub>4</sub>, 1 MgCl<sub>2</sub>, 5 L-glutamic acid, 5 L-malic acid, 0.01 EGTA, 0.1% BSA, and 1 µM Oregon Green BAPTA-6F (Thermo Fisher). pH was adjusted to 7.3 with KOH, and osmolality to 290-300 mOsm/L). Excitation and emission wavelengths were 485/510 nm. 10 µM CaCl<sub>2</sub> was injected per trial. Percent Ca<sup>2+</sup> clearance was calculated as:

$$\left[ 1 - \frac{(F_{ss} - F_{baseline})}{(F_{peak} - F_{baseline})} \right] \times 100\%$$

where  $F_{ss}$  is the steady-state fluorescence level after the mitochondria have taken up the pulse, typically around 3-5 minutes following the Ca<sup>2+</sup> injection,  $F_{baseline}$  is the initial fluorescence level, and  $F_{peak}$  is the maximal fluorescence level immediately following the Ca<sup>2+</sup> injection. Analysis was performed in OriginPro 9 using ANOVA with post-hoc Bonferroni-corrected means comparisons.

### **Histology and Nuclei Counting**

Extracted hearts were incubated in a fixative solution containing 4% paraformaldehyde in PBS for 48 hours at 4°C, and then placed in a 70% ethanol solution. The samples were embedded in paraffin, cut, and stained with Masson's trichrome by the Research Histology core at the Huntsman Cancer Institute (University of Utah). Slides were imaged using a BX51WI microscope (Olympus, Center Valley, PA).

Nuclei density was calculated via automated analysis performed on CellProfiler (v3.1)<sup>69</sup>. The UnmixColors module was used to separate each image into two, one that highlighted nuclei (setting: hematoxylin), and one for cellular staining (setting: eosin). The eosin image was analyzed to determine how much of the image was occupied by cells, to correct for tissue processing and any blank spaces. The hematoxylin image was analyzed to count nuclei. Nuclei density was calculated by dividing the number of nuclei by the area of each image covered by cells. For the eosin image, we used IdentifyPrimaryObjects, MeasureImageAreaOccupied, and the image scale to calculate the area occupied by cells. For the hematoxylin image, to smooth over heterogeneity of staining within each nuclei, we sequentially applied the GaussianFilter, Threshold, and Opening modules. Subsequently, the IdentifyPrimaryObjects module was used to

count nuclei. All images were processed identically. Statistical analysis was performed in R using a Kruskal-Wallis test to establish overall  $p$  value followed by Bonferroni-corrected Dunn's test for pairwise comparisons.

### **Echocardiography**

Echocardiography was performed as described previously<sup>12</sup>. Mice were sedated with inhaled isoflurane, restrained in the supine position, and cleared of chest fur. M-mode images were recorded in short-axis at the level of the papillary muscles, using a Vevo 2100 ultrasound machine equipped with a 55-MHz probe (Visual Sonics, Toronto, Ontario, Canada). Statistical analysis was performed in R using a Kruskal-Wallis test to establish overall  $p$  value followed by Bonferroni-corrected Dunn's test for pairwise comparisons.

### **Island Assay**

Flight capabilities were determined using a modified island assay<sup>70</sup>. We used a rectangular ice pan that held a flypad in the middle. The bottom of the container was filled with cold soap water that reached the top of the flypad without covering it. Clear plastic wrap was placed over half of the container in order to prevent flies from escaping. Female flies were collected within 48 hours of eclosion, and placed on normal fly food in groups of 12. Two days later, flies were tapped to the bottom of the vial, the vial was immediately inverted and flies were tapped onto the flypad in the island. Vials were inspected for any flies remaining after inversion to determine the starting number of flies on the island. Videos were taken of each group, and were manually scored to determine how many flies remained on the flypad every 2 seconds until the 20 second mark was reached. Log-rank (Mantel-Cox) testing was performed in GraphPad Prism 8 with Bonferroni correction for multiple comparisons.

### ***Drosophila* viability assay**

To determine viability, separate groups of male and female flies were counted from at least 3 crosses. Viability was calculated by dividing the number of flies without balancers (experimental group) by the number of flies with balancers (control group) and multiplying by 100 to obtain a percentage. Fischer's Exact Test was performed in GraphPad Prism 8 with Bonferroni correction for multiple comparisons.

### **Cartoons**

Cartoon drawings were based on PDB structures as follows: Complex I, 5LNK<sup>71</sup> and 5LC5<sup>72</sup>; respirasome, 5J4Z<sup>73</sup>; MCU, 6DNF<sup>74</sup>; FRB-Rapamycin-FKBP, 1FRAP<sup>46</sup>; Lon protease, 4YPL<sup>75</sup>.

### **Statistics**

For flow cytometric assays, N refers to individual cells. For electrophysiological assays, N refers to individual mitoplasts. For Duolink imaging, N refers to cells calculated from nuclei staining. For cell culture qPCR, N refers to technical replicates. For animal studies, N refers to individual animals. We considered  $p < 0.05$  statistically significant. Individual tests and software are described in the corresponding sections of the methods.

## ACKNOWLEDGMENTS

We thank Edward Owusu-Ansah, Alex Whitworth, Ronald Davis, and the Bloomington *Drosophila* Stock Center at Indiana University (supported by NIH P40OD018537) for fly stocks, Michael Ryan for the NDUFB10<sup>KO</sup> and NDUFS4<sup>KO</sup> cell lines, John Elrod, Ronald Kahn, and Nils-Göran Larsson for mouse lines, James Marvin and Flow Cytometry Core staff at the University of Utah (supported by NIH P30CA042014), and Derek Warner and DNA Sequencing Core staff at the University of Utah. Support is from the National Institutes of Health (DK110358 [JMP, ARR], UL1TR002538 [CTM], HL124070 [DC], HL141353 [DC, EB], HL007576 [SS]), the Nora Eccles Treadwell Foundation (DC, MTF, SGD, SF), and the University of Utah Driving Out Diabetes, a Larry H. Miller Wellness Initiative (DC, DRE). The content is solely the responsibility of the authors and does not necessarily represent the official views of the National Institutes of Health.

The authors declare no competing interests.

**AUTHOR CONTRIBUTIONS:** Conception: DC, EB, DRE, SS. Design: DC, EB, SS, JMP, DRE, CTM, SF, ARR. Acquisition: EB, SS, JMP, DRE, AMB, XY, MCP, AKH, KF, CTM, SC, AB, RDB, DC. Analysis and interpretation: all authors. EB and DC wrote the manuscript in consultation with all authors.

Correspondence and requests for materials should be addressed to DC.

**Supplemental Table 1. *Drosophila* genotypes.**

Abbreviated Genotype	Female Genotype	Male Genotype
+/+	<i>w/w Berlin</i>	<i>w/Y Berlin</i>
+/ <i>B10<sup>RNAi</sup></i> <i>MCU<sup>DQEQ</sup></i>	<i>w/yw; +/UAS-NDUFB10 RNAi<sup>TRIP-BI29592</sup> UAS-MCU<sup>D206Q,E263Q</sup></i>	<i>w/Y; +/UAS-NDUFB10 RNAi<sup>TRIP-BI29592</sup> UAS-MCU<sup>D206Q,E263Q</sup></i>
MHC>	<i>w/w; MHC-GAL4/+</i>	<i>w/Y; MHC-GAL4/+</i>
MHC> <i>MCU<sup>DQEQ</sup></i>	<i>w/w; MHC-GAL4/UAS-MCU<sup>D206Q,E263Q</sup></i>	<i>w/Y; MHC-GAL4/UAS-MCU<sup>D206Q,E263Q</sup></i>
MHC> <i>B10<sup>RNAi</sup></i>	<i>w/yw; MHC-GAL4/UAS-NDUFB10 RNAi<sup>TRIP-BI29592</sup></i>	<i>w/Y; MHC-GAL4/UAS-NDUFB10 RNAi<sup>TRIP-BI29592</sup></i>
MHC> <i>B10<sup>RNAi</sup></i> <i>MCU<sup>DQEQ</sup></i>	<i>w/yw; MHC-GAL4/UAS-NDUFB10 RNAi<sup>TRIP-BI29592</sup> UAS-MCU<sup>D206Q,E263Q</sup></i>	<i>w/Y; MHC-GAL4/UAS-NDUFB10 RNAi<sup>TRIP-BI29592</sup> UAS-MCU<sup>D206Q,E263Q</sup></i>
+/ <i>MCU<sup>1</sup> B10<sup>RNAi</sup></i>	<i>w/yw; +/MCU<sup>1</sup> UAS-NDUFB10 RNAi<sup>TRIP-BI29592</sup></i>	<i>w/Y; +/MCU<sup>1</sup> UAS-NDUFB10 RNAi<sup>TRIP-BI29592</sup></i>
<i>MCU<sup>1</sup>/MCU<sup>1</sup></i>	<i>w/w; MCU<sup>1</sup>/MCU<sup>1</sup></i>	<i>w/Y; MCU<sup>1</sup>/MCU<sup>1</sup></i>
MHC> <i>B10<sup>RNAi</sup></i> <i>MCU<sup>1</sup>/MCU<sup>1</sup></i>	<i>w/yw; MHC-GAL4 MCU<sup>1</sup>/MCU<sup>1</sup> UAS-NDUFB10 RNAi<sup>TRIP-BI29592</sup></i>	<i>w/Y; MHC-GAL4 MCU<sup>1</sup>/MCU<sup>1</sup> UAS-NDUFB10 RNAi<sup>TRIP-BI29592</sup></i>
+/ <i>A13<sup>RNAi</sup></i> <i>MCU<sup>DQEQ</sup></i>	<i>w/yw; +/UAS-NDUFA13 RNAi<sup>TRIP-BI43279</sup> UAS-MCU<sup>D206Q,E263Q</sup></i>	<i>w/Y; +/UAS-NDUFA13 RNAi<sup>TRIP-BI43279</sup> UAS-MCU<sup>D206Q,E263Q</sup></i>
MHC> <i>A13<sup>RNAi</sup></i>	<i>w/yw; MHC-GAL4/UAS-NDUFA13 RNAi<sup>TRIP-BI43279</sup></i>	<i>w/Y; MHC-GAL4/UAS-NDUFA13 RNAi<sup>TRIP-BI43279</sup></i>
MHC> <i>A13<sup>RNAi</sup></i> <i>MCU<sup>DQEQ</sup></i>	<i>w/yw; MHC-GAL4/UAS-NDUFA13 RNAi<sup>TRIP-BI43279</sup> UAS-MCU<sup>D206Q,E263Q</sup></i>	<i>w/Y; MHC-GAL4/UAS-NDUFA13 RNAi<sup>TRIP-BI43279</sup> UAS-MCU<sup>D206Q,E263Q</sup></i>
MHC> <i>MCU<sup>WT</sup></i> <i>B10<sup>RNAi</sup></i> <i>MCU<sup>1</sup>/MCU<sup>1</sup></i> MHC> <i>MCU</i>	<i>w/w; UAS-MCU<sup>WT</sup>/+; MCU<sup>1</sup> MHC-GAL4/MCU<sup>1</sup> UAS-NDUFB10 RNAi<sup>TRIP-BI29592</sup></i>	<i>w/Y; UAS-MCU<sup>WT</sup>/+; MCU<sup>1</sup> MHC-GAL4/MCU<sup>1</sup> UAS-NDUFB10 RNAi<sup>TRIP-BI29592</sup></i>

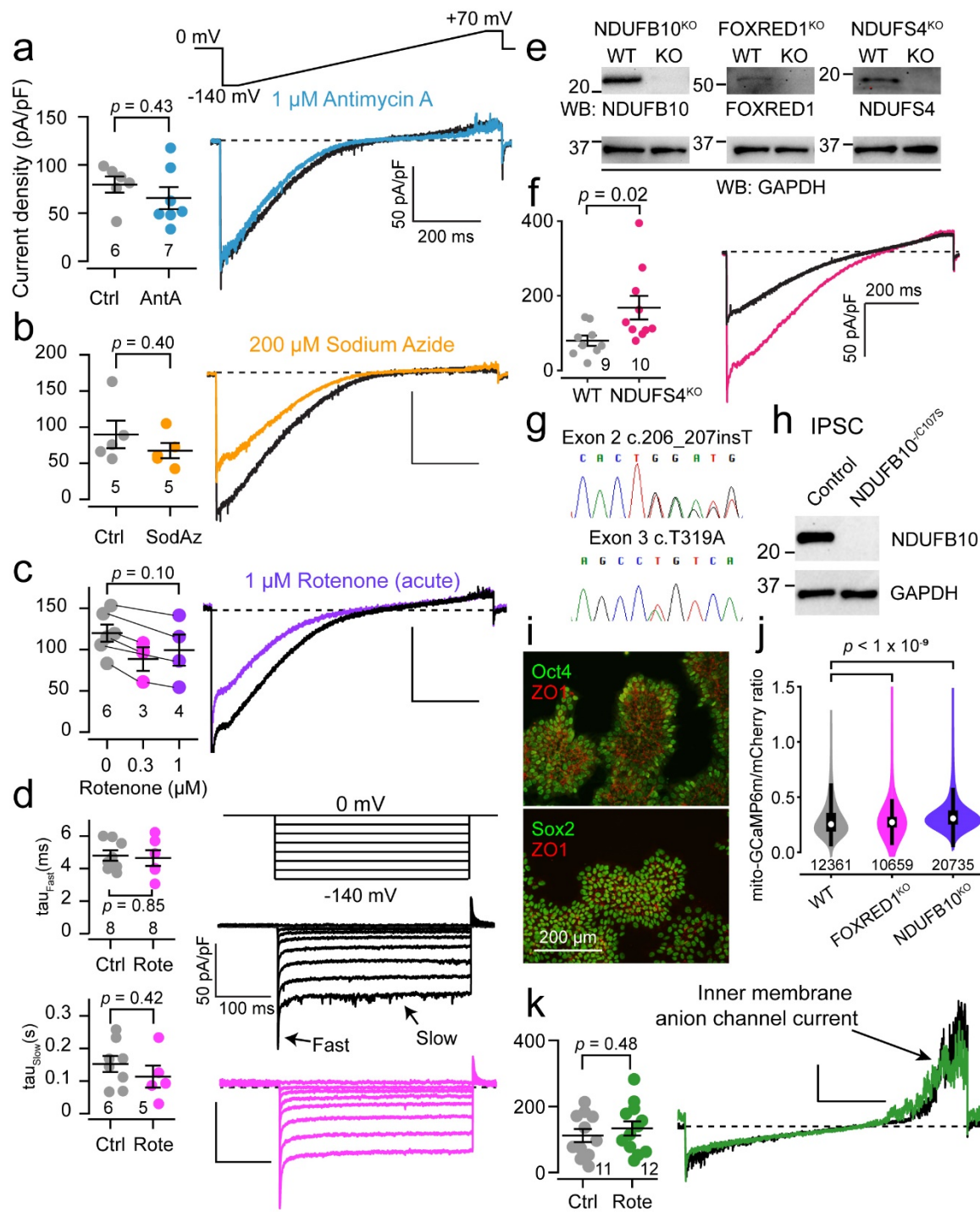


**Figure S1. Further characterization of pharmacological Complex I dysfunction.** **A-D**, Left, summary data. Right, exemplar  $I_{MiCa}$  traces. **A**, Inhibition of Complex III with 1  $\mu$ M antimycin A does not alter  $I_{MiCa}$ . **B**, Inhibition of Complex IV with 200  $\mu$ M sodium azide does not alter  $I_{MiCa}$ . **C**, Acute addition of 1  $\mu$ M rotenone during electrophysiological recordings does not increase  $I_{MiCa}$ . Lines connect individual trials before and after rotenone addition. **D**, Chronic Complex I inhibition with rotenone does not alter  $I_{MiCa}$  fast or slow inactivation kinetics. **E**, NDUFB10, FOXRED1, and

NDUFS4 protein depletion in NDUFB10<sup>KO</sup>, FOXRED1<sup>KO</sup>, and NDUFS4<sup>KO</sup> cells. **F.** Enhanced I<sub>MiCa</sub> in NDUFS4<sup>KO</sup> cells. **G.** NDUFB10 inactivating mutations are preserved in patient-derived iPSCs. **H.** NDUFB10 protein depletion in NDUFB10<sup>-/C107S</sup> iPSCs. **I.** Confirmation that stem cell markers are expressed in NDUFB10<sup>-/C107S</sup> iPSCs. **J.** Increased mitochondrial Ca<sup>2+</sup> levels in NDUFB10<sup>KO</sup> and FOXRED1<sup>KO</sup> cells. **K.** Inner membrane anion channel currents are unaltered by chronic rotenone treatment.

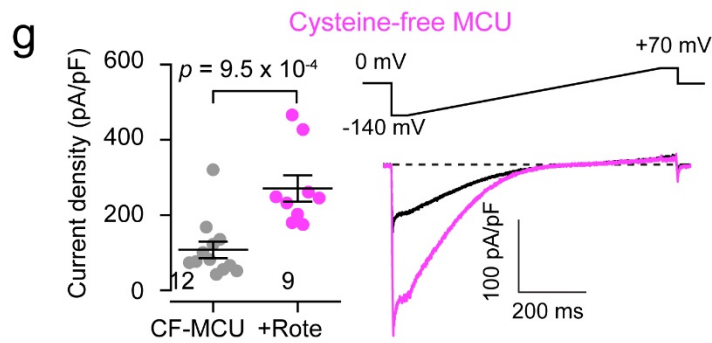
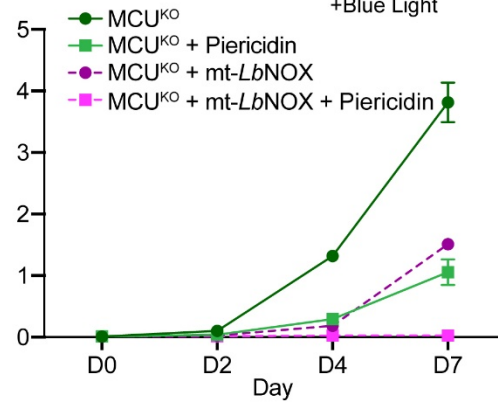
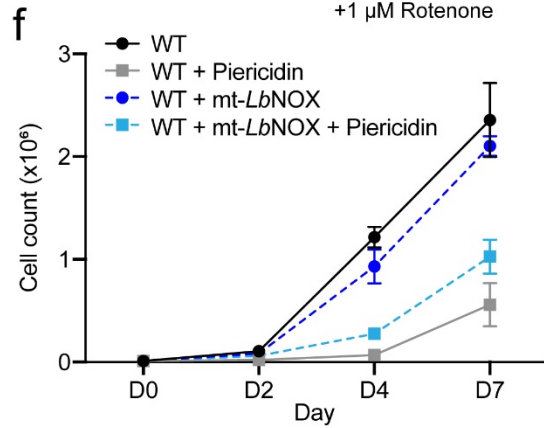
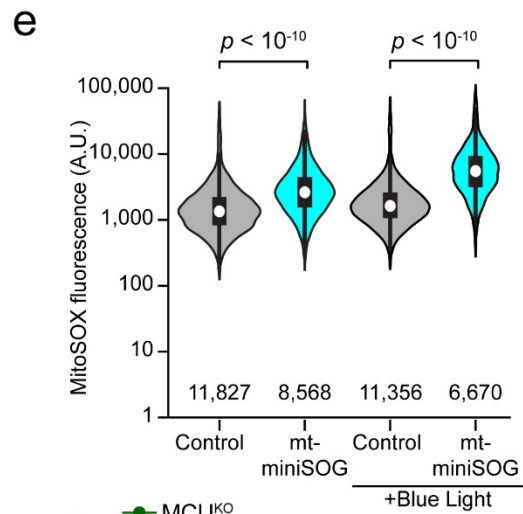
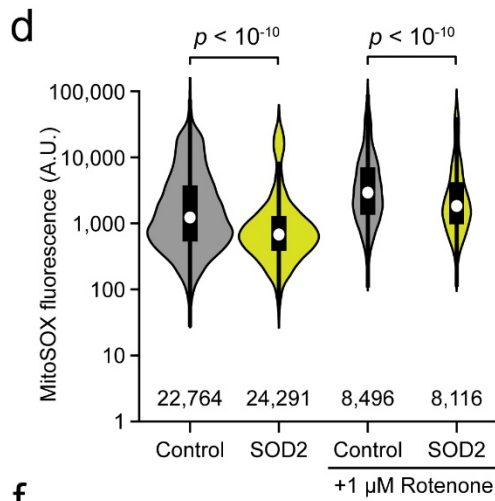
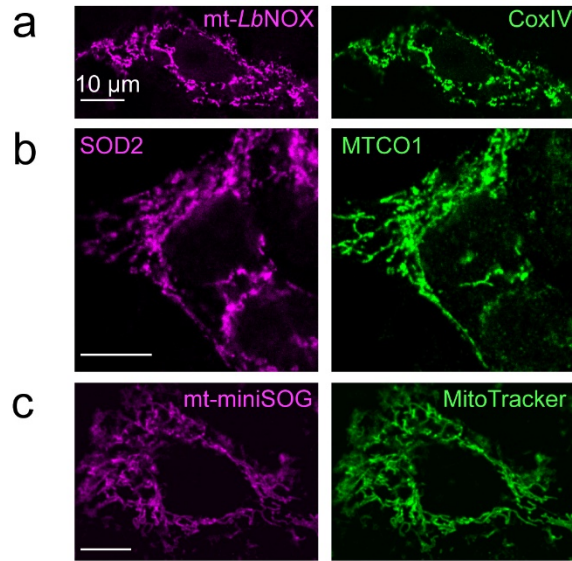


**Figure S2. Tools used to identify the ROS signal altering uniporter function.** **A.** Immunocytochemistry to show mitochondrial targeting of mt-*LbNOX* (left). CoxIV antibody labels mitochondria. **B.** Immunocytochemistry of SOD2 overexpression. MTCO1 antibody labels mitochondria. **C.** Mito-miniSOG fluorescence in live cells. MitoTracker labels mitochondria. **D.** Mitochondrial SOD2 overexpression blunts ROS production measured by MitoSOX flow cytometry. **E.** Mitochondrial miniSOG expression enhances ROS production after blue light exposure. **F.** Effect of mt-*LbNOX* expression on cell proliferation inhibited by piericidin in WT or MCU<sup>KO</sup> cells. (N = 3 replicates). **G.** I<sub>MiCa</sub> enhancement persists after Complex I dysfunction in MCU<sup>KO</sup> cells expressing CF-MCU-Flag.

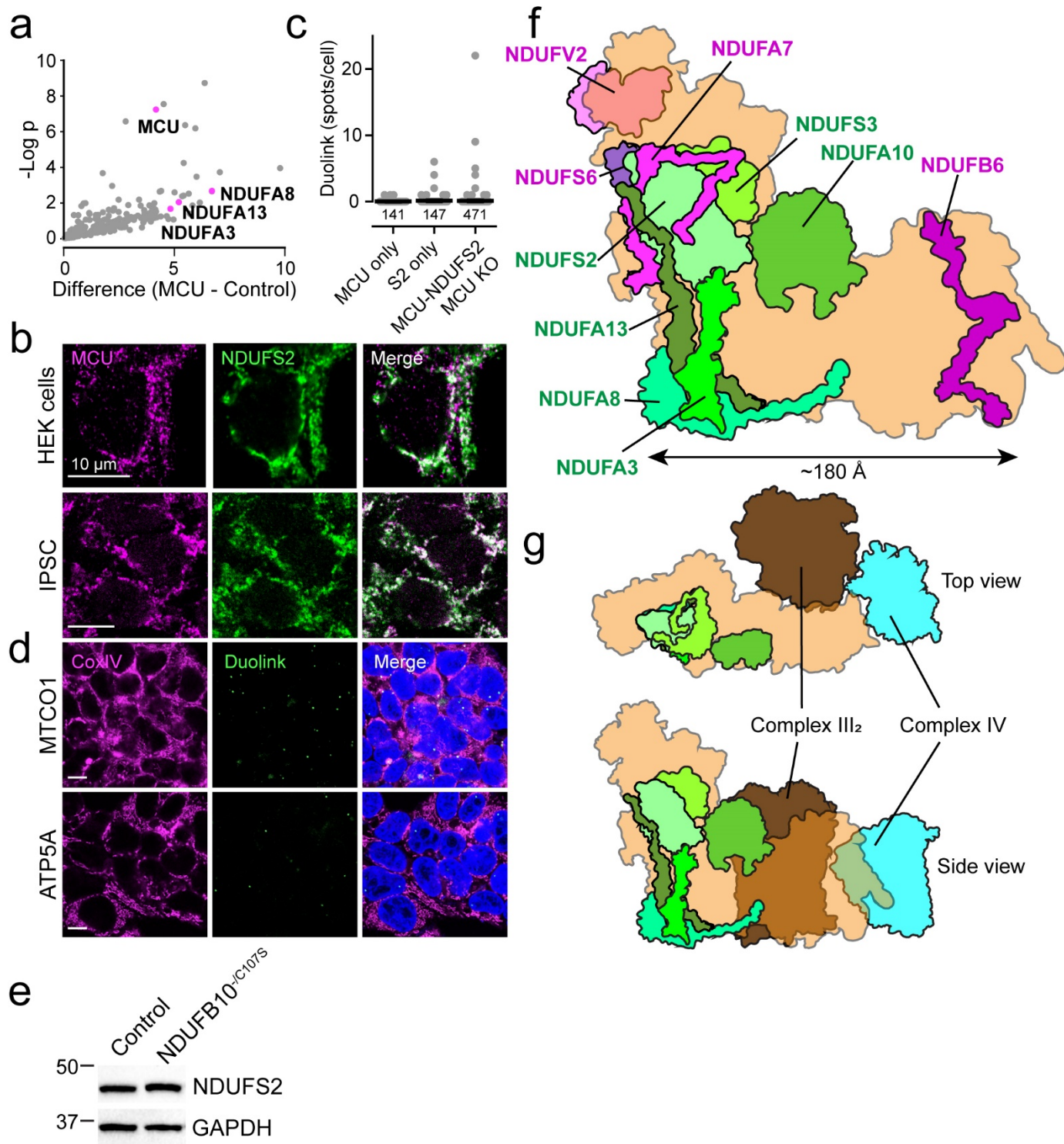


**Figure S3. Further characterization of MCU-Complex I biochemical interaction.** **A.** Plot of proteins detected in MCU-Flag proteomic screen. **B.** Rabbit anti-MCU and mouse anti-NDUFS localize to mitochondria when used concurrently in HEK293T cells or iPSCs. **C.** Absence of substantial Duolink labeling in controls. 98%, 93%, and 98% of the cells had no Duolink spots for

MCU only, S2 only, and MCU KO, respectively. **D.** Specificity of interaction with respirasome via Duolink assay using Complex IV component MTCO1. Much weaker Duolink signal when targeting the ATP synthase using ATP5A. **E.** Preserved NDUFS2 levels in patient-derived NDUFB10<sup>-/C107S</sup> iPSCs. **F.** Cartoon overview of MCU-Complex I interaction. Complex I subunits that interact with MCU are labeled green, while those that failed to interact are magenta. **G.** Top and side views of the respirasome (CI-CIII<sub>2</sub>-CIV). The MCU-interacting subunits of Complex I form a surface cluster and are not sterically hindered in the respirasome by Complex III or IV, which are on the opposite sides.

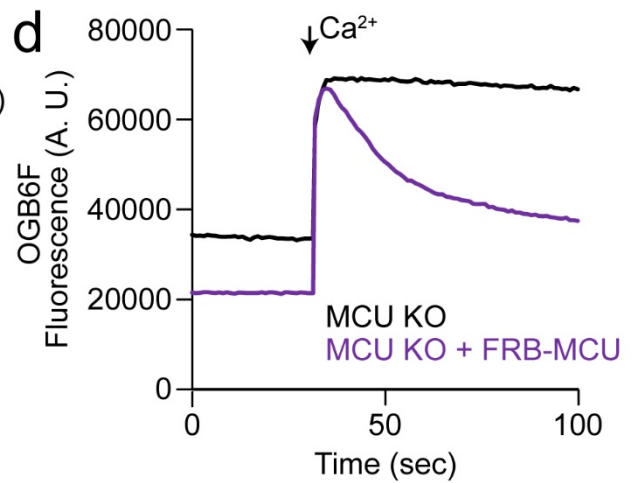
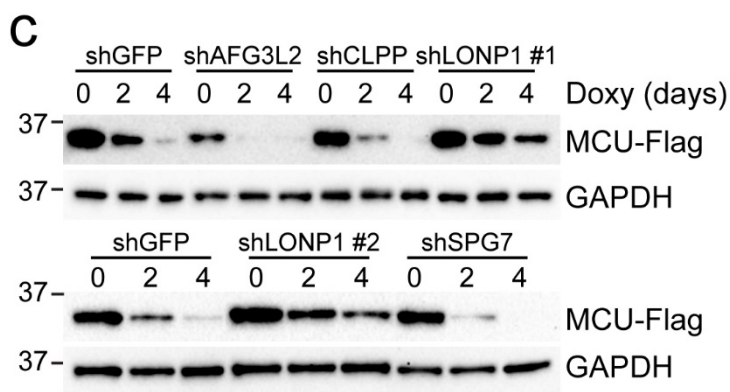
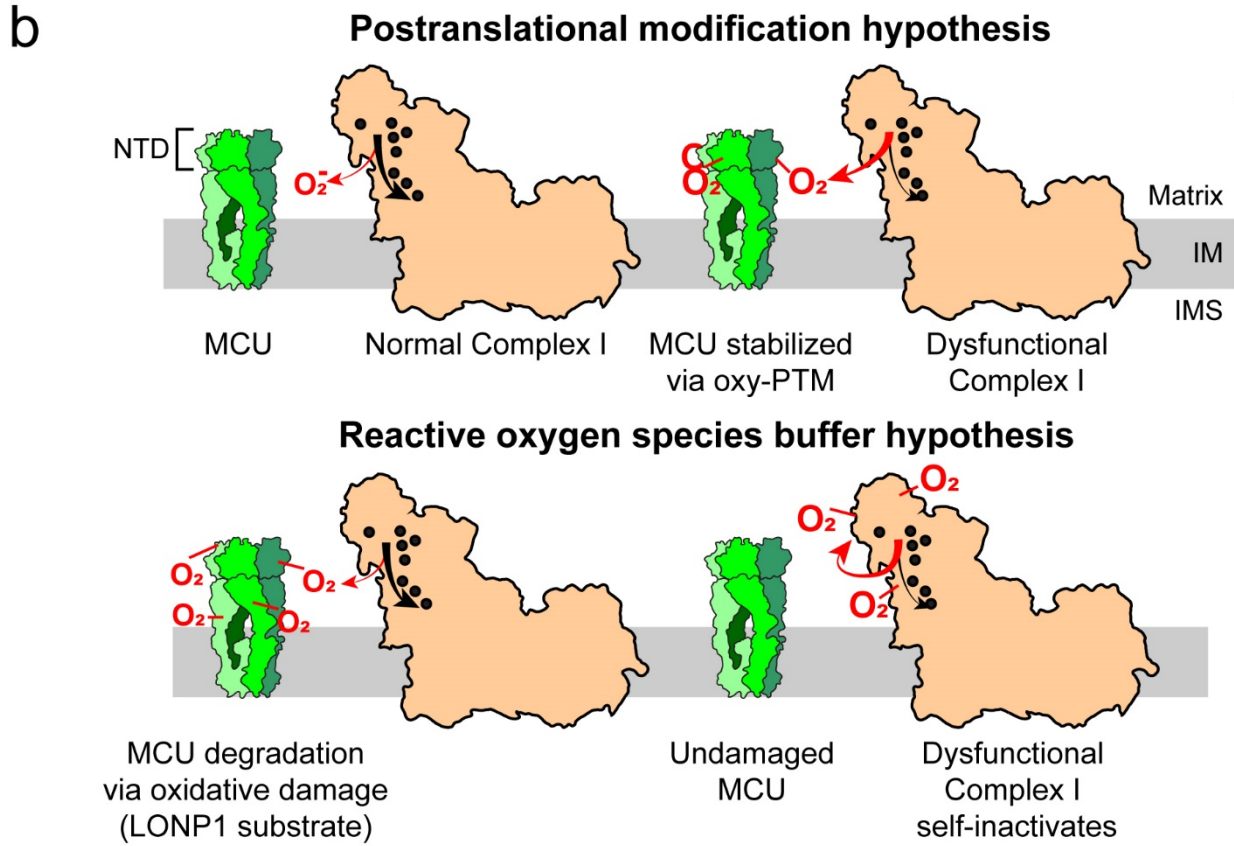
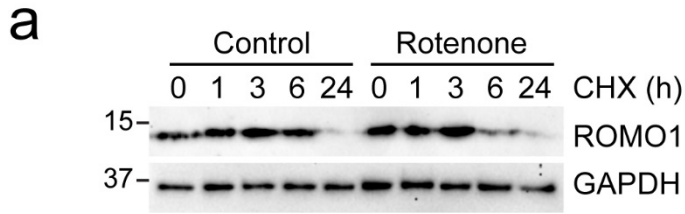


**Figure S4. Further analysis of MCU stability.** **A.** ROMO1 stability is unaffected by rotenone treatment. **B.** Hypotheses for Complex I control of MCU stability. In the PTM hypothesis, ROS escaping Complex I produces specific oxidative modifications (oxy-PTM) on MCU that stabilize it. In the CLIPT hypothesis, under normal conditions MCU is turned over by quality control proteases due to constant promiscuous modifications from basal ROS leak from Complex I. Complex I dysfunction produces a self-inactivating ROS burst that prevents further MCU oxidative damage, thus stabilizing it. **C.** MCU-Flag stability after RNAi of quality-control proteases reveals LONP1-mediated MCU degradation. shRNA produced 88-96% inhibition of the corresponding transcripts. **D.** Mitochondrial  $\text{Ca}^{2+}$  uptake is absent in digitonin-permeabilized  $\text{MCU}^{\text{KO}}$  cells but present after expression of FRB-MCU in these.  $\text{Ca}^{2+}$  fluorescence measured with Oregon Green BAPTA 6F (OGB6F). Arrow indicates 10  $\mu\text{M}$   $\text{Ca}^{2+}$  pulse.

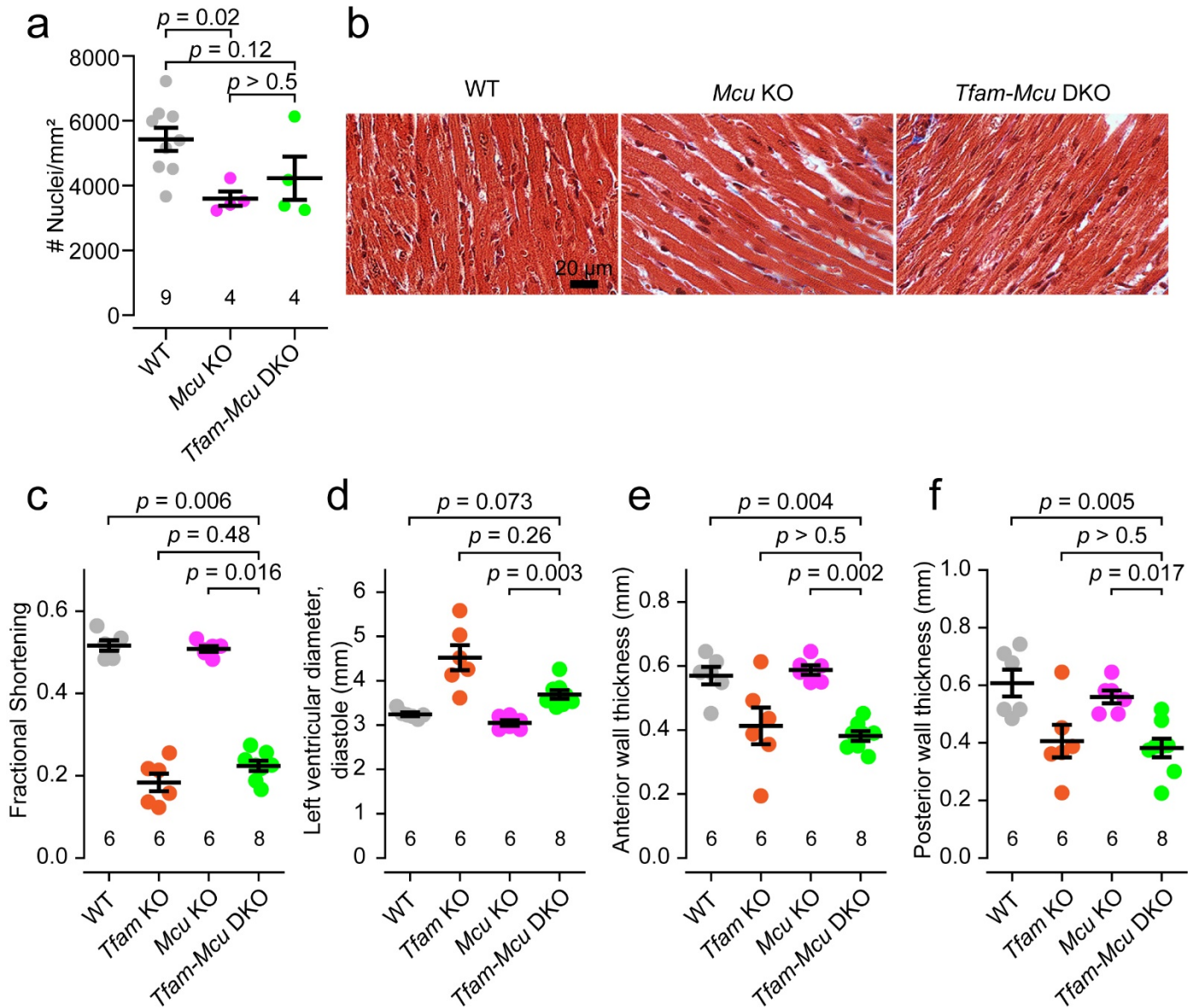


**Figure S5. Further analysis of *Tfam-Mcu* DKO mice. A.** Automated analysis of nuclei density in immunohistological slices of cardiac tissue. N refers to number of mice studied. **B.** Masson's trichrome staining of mid-ventricular heart reveals no excess infiltrates or fibrosis in *Mcu* KO or *Tfam-Mcu* DKO mice. **C-F.** Echocardiographic parameters for the indicated genotypes obtained from M-mode imaging. **C.** Fractional shortening. **D.** Left ventricular chamber diameter. **E, F.** Ventricular wall thicknesses.

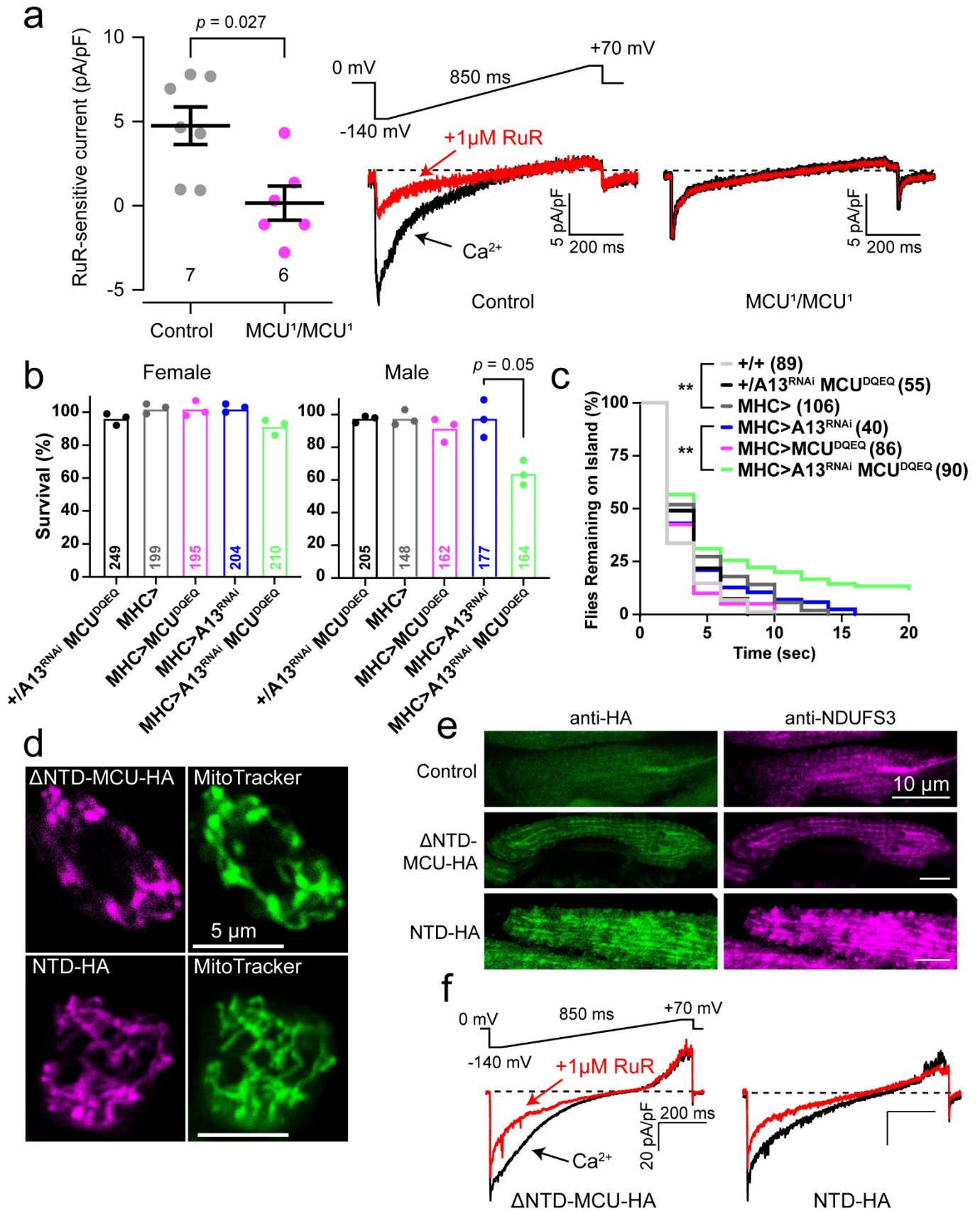


**Figure S6. Further data on genetic interaction between MCU and Complex I.** **A.** Summary and exemplars for ruthenium-red sensitive  $I_{\text{MiCa}}$  in wild-type and  $MCU^1/MCU^1$  flies. **B.** Survival for  $NDUFA13^{\text{RNAi}}$  and  $MCU^{\text{DQEQ}}$  crosses. **C.** Island assay. **D.** *Drosophila* S2 cell expressing  $\Delta\text{NTD-MCU}$  and MCU NTD fragment. **E.** *Drosophila* flight muscle showing expression of  $\Delta\text{NTD-MCU}$  and MCU NTD. **F.** Expression of  $\Delta\text{NTD-MCU}$  produces ruthenium-red sensitive currents in *Drosophila* MCU knockout ( $MCU^1/MCU^1$ ) mitochondria (left).  $\text{Ca}^{2+}$  current exemplar after expression of NTD-HA (right).

1. Glancy, B. & Balaban, R.S. Role of mitochondrial Ca<sup>2+</sup> in the regulation of cellular energetics. *Biochemistry* **51**, 2959-2973 (2012).
2. Territo, P.R., Mootha, V.K., French, S.A. & Balaban, R.S. Ca<sup>2+</sup> activation of heart mitochondrial oxidative phosphorylation: role of the F<sub>0</sub>/F<sub>1</sub>-ATPase. *American journal of physiology. Cell physiology* **278**, C423-435 (2000).
3. El-Hattab, A.W. & Scaglia, F. Mitochondrial Cardiomyopathies. *Front Cardiovasc Med* **3**, 25 (2016).
4. Meyers, D.E., Basha, H.I. & Koenig, M.K. Mitochondrial cardiomyopathy: pathophysiology, diagnosis, and management. *Tex Heart Inst J* **40**, 385-394 (2013).
5. Aydin, J. *et al.* Increased mitochondrial Ca<sup>2+</sup> and decreased sarcoplasmic reticulum Ca<sup>2+</sup> in mitochondrial myopathy. *Human molecular genetics* **18**, 278-288 (2009).
6. Brini, M. *et al.* A calcium signaling defect in the pathogenesis of a mitochondrial DNA inherited oxidative phosphorylation deficiency. *Nat Med* **5**, 951-954 (1999).
7. Granatiero, V. *et al.* Reduced mitochondrial Ca<sup>2+</sup> transients stimulate autophagy in human fibroblasts carrying the 13514A>G mutation of the ND5 subunit of NADH dehydrogenase. *Cell death and differentiation* **23**, 231-241 (2016).
8. Willems, P.H. *et al.* Mitochondrial Ca<sup>2+</sup> homeostasis in human NADH:ubiquinone oxidoreductase deficiency. *Cell calcium* **44**, 123-133 (2008).
9. Jana, F. *et al.* Complex I and II are required for normal mitochondrial Ca<sup>2+</sup> homeostasis. *Mitochondrion* **49**, 73-82 (2019).
10. Karamanlidis, G. *et al.* Mitochondrial complex I deficiency increases protein acetylation and accelerates heart failure. *Cell metabolism* **18**, 239-250 (2013).
11. McKenzie, M. & Duchen, M.R. Impaired Cellular Bioenergetics Causes Mitochondrial Calcium Handling Defects in MT-ND5 Mutant Cybrids. *PloS one* **11**, e0154371 (2016).
12. Sommakia, S. *et al.* Mitochondrial cardiomyopathies feature increased uptake and diminished efflux of mitochondrial calcium. *Journal of molecular and cellular cardiology* **113**, 22-32 (2017).
13. Wang, J. *et al.* Dilated cardiomyopathy and atrioventricular conduction blocks induced by heart-specific inactivation of mitochondrial DNA gene expression. *Nature genetics* **21**, 133-137 (1999).
14. Baughman, J.M. *et al.* Integrative genomics identifies MCU as an essential component of the mitochondrial calcium uniporter. *Nature* **476**, 341-345 (2011).
15. Chaudhuri, D., Sancak, Y., Mootha, V.K. & Clapham, D.E. MCU encodes the pore conducting mitochondrial calcium currents. *eLife* **2**, e00704 (2013).

16. De Stefani, D., Raffaello, A., Teardo, E., Szabo, I. & Rizzuto, R. A forty-kilodalton protein of the inner membrane is the mitochondrial calcium uniporter. *Nature* **476**, 336-340 (2011).
17. Kirichok, Y., Krapivinsky, G. & Clapham, D.E. The mitochondrial calcium uniporter is a highly selective ion channel. *Nature* **427**, 360-364 (2004).
18. Luongo, T.S. *et al.* The Mitochondrial Calcium Uniporter Matches Energetic Supply with Cardiac Workload during Stress and Modulates Permeability Transition. *Cell reports* **12**, 23-34 (2015).
19. Kwong, J.Q. *et al.* The Mitochondrial Calcium Uniporter Selectively Matches Metabolic Output to Acute Contractile Stress in the Heart. *Cell reports* **12**, 15-22 (2015).
20. Pan, X. *et al.* The physiological role of mitochondrial calcium revealed by mice lacking the mitochondrial calcium uniporter. *Nature cell biology* **15**, 1464-1472 (2013).
21. Valsecchi, F., Esseling, J.J., Koopman, W.J. & Willems, P.H. Calcium and ATP handling in human NADH:ubiquinone oxidoreductase deficiency. *Biochimica et biophysica acta* **1792**, 1130-1137 (2009).
22. Kowaltowski, A.J. *et al.* Mitochondrial morphology regulates organellar Ca(2+) uptake and changes cellular Ca(2+) homeostasis. *FASEB journal : official publication of the Federation of American Societies for Experimental Biology* **33**, 13176-13188 (2019).
23. Sancak, Y. *et al.* EMRE is an essential component of the mitochondrial calcium uniporter complex. *Science* **342**, 1379-1382 (2013).
24. Stroud, D.A. *et al.* Accessory subunits are integral for assembly and function of human mitochondrial complex I. *Nature* **538**, 123-126 (2016).
25. Titov, D.V. *et al.* Complementation of mitochondrial electron transport chain by manipulation of the NAD<sup>+</sup>/NADH ratio. *Science* **352**, 231-235 (2016).
26. King, M.P. & Attardi, G. Isolation of human cell lines lacking mitochondrial DNA. *Methods in enzymology* **264**, 304-313 (1996).
27. Formosa, L.E. *et al.* Characterization of mitochondrial FOXRED1 in the assembly of respiratory chain complex I. *Human molecular genetics* **24**, 2952-2965 (2015).
28. Friederich, M.W. *et al.* Mutations in the accessory subunit NDUFB10 result in isolated complex I deficiency and illustrate the critical role of intermembrane space import for complex I holoenzyme assembly. *Human molecular genetics* **26**, 702-716 (2017).
29. Garcia, C.J., Khajeh, J., Coulanges, E., Chen, E.I. & Owusu-Ansah, E. Regulation of Mitochondrial Complex I Biogenesis in Drosophila Flight Muscles. *Cell reports* **20**, 264-278 (2017).
30. Pryde, K.R., Taanman, J.W. & Schapira, A.H. A LON-ClpP Proteolytic Axis Degrades Complex I to Extinguish ROS Production in Depolarized Mitochondria. *Cell reports* **17**, 2522-2531 (2016).

31. Chen, Y.R., Chen, C.L., Zhang, L., Green-Church, K.B. & Zweier, J.L. Superoxide generation from mitochondrial NADH dehydrogenase induces self-inactivation with specific protein radical formation. *The Journal of biological chemistry* **280**, 37339-37348 (2005).
32. Zhao, Y. *et al.* SoNar, a Highly Responsive NAD<sup>+</sup>/NADH Sensor, Allows High-Throughput Metabolic Screening of Anti-tumor Agents. *Cell metabolism* **21**, 777-789 (2015).
33. Shu, X. *et al.* A genetically encoded tag for correlated light and electron microscopy of intact cells, tissues, and organisms. *PLoS biology* **9**, e1001041 (2011).
34. Dong, Z. *et al.* Mitochondrial Ca<sup>2+</sup> Uniporter Is a Mitochondrial Luminal Redox Sensor that Augments MCU Channel Activity. *Molecular cell* **65**, 1014-1028 e1017 (2017).
35. Wang, Y. *et al.* Structural Mechanism of EMRE-Dependent Gating of the Human Mitochondrial Calcium Uniporter. *Cell* **177**, 1252-1261 e1213 (2019).
36. Lee, Y. *et al.* Structure and function of the N-terminal domain of the human mitochondrial calcium uniporter. *EMBO reports* **16**, 1318-1333 (2015).
37. Lee, S.K. *et al.* Structural Insights into Mitochondrial Calcium Uniporter Regulation by Divalent Cations. *Cell Chem Biol* **23**, 1157-1169 (2016).
38. Muller, F.L., Liu, Y. & Van Remmen, H. Complex III releases superoxide to both sides of the inner mitochondrial membrane. *The Journal of biological chemistry* **279**, 49064-49073 (2004).
39. Guarani, V. *et al.* TIMMDC1/C3orf1 functions as a membrane-embedded mitochondrial complex I assembly factor through association with the MCI1A complex. *Mol Cell Biol* **34**, 847-861 (2014).
40. Antonicka, H. *et al.* A High-Density Human Mitochondrial Proximity Interaction Network. *Cell metabolism* **32**, 479-497 e479 (2020).
41. Bajar, B.T., Wang, E.S., Zhang, S., Lin, M.Z. & Chu, J. A Guide to Fluorescent Protein FRET Pairs. *Sensors (Basel)* **16** (2016).
42. Dieteren, C.E. *et al.* Subunit-specific incorporation efficiency and kinetics in mitochondrial complex I homeostasis. *The Journal of biological chemistry* **287**, 41851-41860 (2012).
43. Lee, S.R., Sang, L. & Yue, D.T. Uncovering Aberrant Mutant PKA Function with Flow Cytometric FRET. *Cell reports* **14**, 3019-3029 (2016).
44. Jarvius, M. *et al.* In situ detection of phosphorylated platelet-derived growth factor receptor beta using a generalized proximity ligation method. *Mol Cell Proteomics* **6**, 1500-1509 (2007).
45. Gu, X. *et al.* SAMTOR is an S-adenosylmethionine sensor for the mTORC1 pathway. *Science* **358**, 813-818 (2017).

46. Choi, J., Chen, J., Schreiber, S.L. & Clardy, J. Structure of the FKBP12-rapamycin complex interacting with the binding domain of human FRAP. *Science* **273**, 239-242 (1996).
47. Hansson, A. *et al.* A switch in metabolism precedes increased mitochondrial biogenesis in respiratory chain-deficient mouse hearts. *Proceedings of the National Academy of Sciences of the United States of America* **101**, 3136-3141 (2004).
48. Li, H. *et al.* Genetic modification of survival in tissue-specific knockout mice with mitochondrial cardiomyopathy. *Proceedings of the National Academy of Sciences of the United States of America* **97**, 3467-3472 (2000).
49. Tavi, P., Hansson, A., Zhang, S.J., Larsson, N.G. & Westerblad, H. Abnormal Ca(2+) release and catecholamine-induced arrhythmias in mitochondrial cardiomyopathy. *Human molecular genetics* **14**, 1069-1076 (2005).
50. Zhang, D. *et al.* Mitochondrial Cardiomyopathy Caused by Elevated Reactive Oxygen Species and Impaired Cardiomyocyte Proliferation. *Circulation research* **122**, 74-87 (2018).
51. Gaussin, V. *et al.* Endocardial cushion and myocardial defects after cardiac myocyte-specific conditional deletion of the bone morphogenetic protein receptor ALK3. *Proceedings of the National Academy of Sciences of the United States of America* **99**, 2878-2883 (2002).
52. Rodenburg, R.J. Mitochondrial complex I-linked disease. *Biochimica et biophysica acta* **1857**, 938-945 (2016).
53. Tufi, R. *et al.* Comprehensive Genetic Characterization of Mitochondrial Ca(2+) Uniporter Components Reveals Their Different Physiological Requirements In Vivo. *Cell reports* **27**, 1541-1550 e1545 (2019).
54. Fieni, F., Bae Lee, S., Jan, Y.N. & Kirichok, Y. Activity of the mitochondrial calcium uniporter varies greatly between tissues. *Nature communications* **3**, 1317 (2012).
55. Drago, I. & Davis, R.L. Inhibiting the Mitochondrial Calcium Uniporter during Development Impairs Memory in Adult Drosophila. *Cell reports* **16**, 2763-2776 (2016).
56. Altamimi, T.R. *et al.* Cardiac-specific deficiency of the mitochondrial calcium uniporter augments fatty acid oxidation and functional reserve. *Journal of molecular and cellular cardiology* **127**, 223-231 (2019).
57. Li, Y., Calvo, S.E., Gutman, R., Liu, J.S. & Mootha, V.K. Expansion of biological pathways based on evolutionary inference. *Cell* **158**, 213-225 (2014).
58. Adlakha, J. *et al.* Characterization of MCU-Binding Proteins MCUR1 and CCDC90B - Representatives of a Protein Family Conserved in Prokaryotes and Eukaryotic Organelles. *Structure* **27**, 464-475 e466 (2019).
59. Chaudhuri, D., Artiga, D.J., Abiria, S.A. & Clapham, D.E. Mitochondrial calcium uniporter regulator 1 (MCUR1) regulates the calcium threshold for the mitochondrial permeability

- transition. *Proceedings of the National Academy of Sciences of the United States of America* **113**, E1872-1880 (2016).
60. Oxenoid, K. *et al.* Architecture of the mitochondrial calcium uniporter. *Nature* **533**, 269-273 (2016).
  61. MacEwen, M.J.S. *et al.* Molecular basis of EMRE-dependence of the human mitochondrial calcium uniporter. *bioRxiv*, 637918 (2019).
  62. Inoue, T., Heo, W.D., Grimley, J.S., Wandless, T.J. & Meyer, T. An inducible translocation strategy to rapidly activate and inhibit small GTPase signaling pathways. *Nat Methods* **2**, 415-418 (2005).
  63. Vernochet, C. *et al.* Adipose-Specific Deletion of TFAM Increases Mitochondrial Oxidation and Protects Mice against Obesity and Insulin Resistance. *Cell metabolism* **16**, 765-776 (2012).
  64. Agah, R. *et al.* Gene recombination in postmitotic cells. Targeted expression of Cre recombinase provokes cardiac-restricted, site-specific rearrangement in adult ventricular muscle in vivo. *The Journal of clinical investigation* **100**, 169-179 (1997).
  65. Wang, X., Spandidos, A., Wang, H. & Seed, B. PrimerBank: a PCR primer database for quantitative gene expression analysis, 2012 update. *Nucleic Acids Res* **40**, D1144-1149 (2012).
  66. Krzystek-Korpacka, M., Diakowska, D., Bania, J. & Gamian, A. Expression stability of common housekeeping genes is differently affected by bowel inflammation and cancer: implications for finding suitable normalizers for inflammatory bowel disease studies. *Inflamm Bowel Dis* **20**, 1147-1156 (2014).
  67. Warren, J.S. *et al.* Histone methyltransferase Smyd1 regulates mitochondrial energetics in the heart. *Proceedings of the National Academy of Sciences of the United States of America* **115**, E7871-E7880 (2018).
  68. Shibayama, J. *et al.* Metabolic remodeling in moderate synchronous versus dyssynchronous pacing-induced heart failure: integrated metabolomics and proteomics study. *PloS one* **10**, e0118974 (2015).
  69. McQuin, C. *et al.* CellProfiler 3.0: Next-generation image processing for biology. *PLoS biology* **16**, e2005970 (2018).
  70. Eidhof, I. *et al.* High-throughput Analysis of Locomotor Behavior in the Drosophila Island Assay. *J Vis Exp* (2017).
  71. Fiedorczuk, K. *et al.* Atomic structure of the entire mammalian mitochondrial complex I. *Nature* **538**, 406-410 (2016).
  72. Zhu, J., Vinothkumar, K.R. & Hirst, J. Structure of mammalian respiratory complex I. *Nature* **536**, 354-358 (2016).

73. Letts, J.A., Fiedorczuk, K. & Sazanov, L.A. The architecture of respiratory supercomplexes. *Nature* **537**, 644-648 (2016).
74. Baradaran, R., Wang, C., Siliciano, A.F. & Long, S.B. Cryo-EM structures of fungal and metazoan mitochondrial calcium uniporters. *Nature* **559**, 580-584 (2018).
75. Lin, C.C. *et al.* Structural Insights into the Allosteric Operation of the Lon AAA+ Protease. *Structure* **24**, 667-675 (2016).

# Figures

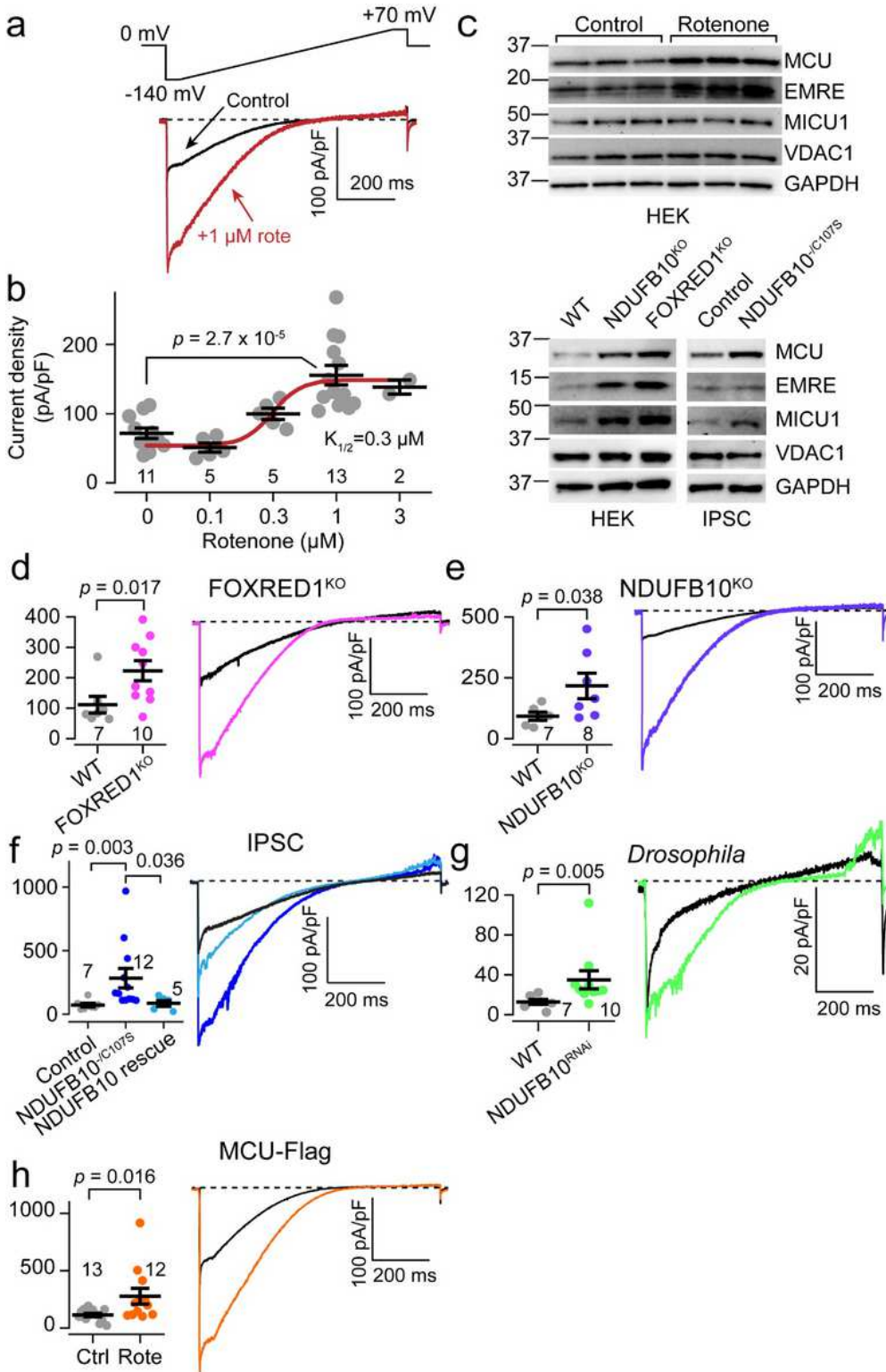


**Figure 1**

Complex I dysfunction increases IMiCa. A. Top, voltage ramp protocol. Bottom, Exemplar IMiCa traces are larger after chronic 1  $\mu\text{M}$  rotenone treatment in HEK293T cells. B. Summary rotenone dose-response curve. Black lines represent mean  $\pm$  SEM and N values are listed in the summary graph here and

throughout. C. Immunoblotting reveals increased uniporter subunit proteins after Complex I impairment in HEK293T, NDUFB10KO, FOXRED1KO, and patient-derived iPSCs (NDUFB10-/C107S) compared to controls. VDAC1 and GAPDH are loading controls. Here and throughout, representative blots from at least 3 replicates are shown. D-G. Each panel contains the summary (left) and exemplar (right) for peak inward IMiCa in FOXRED1KO (D), NDUFB10KO (E), patient-derived iPSCs (F), and *Drosophila* NDUFB10RNAi (G), compared to controls (black). H. IMiCa is increased in cells expressing MCU-Flag after Complex I impairment.

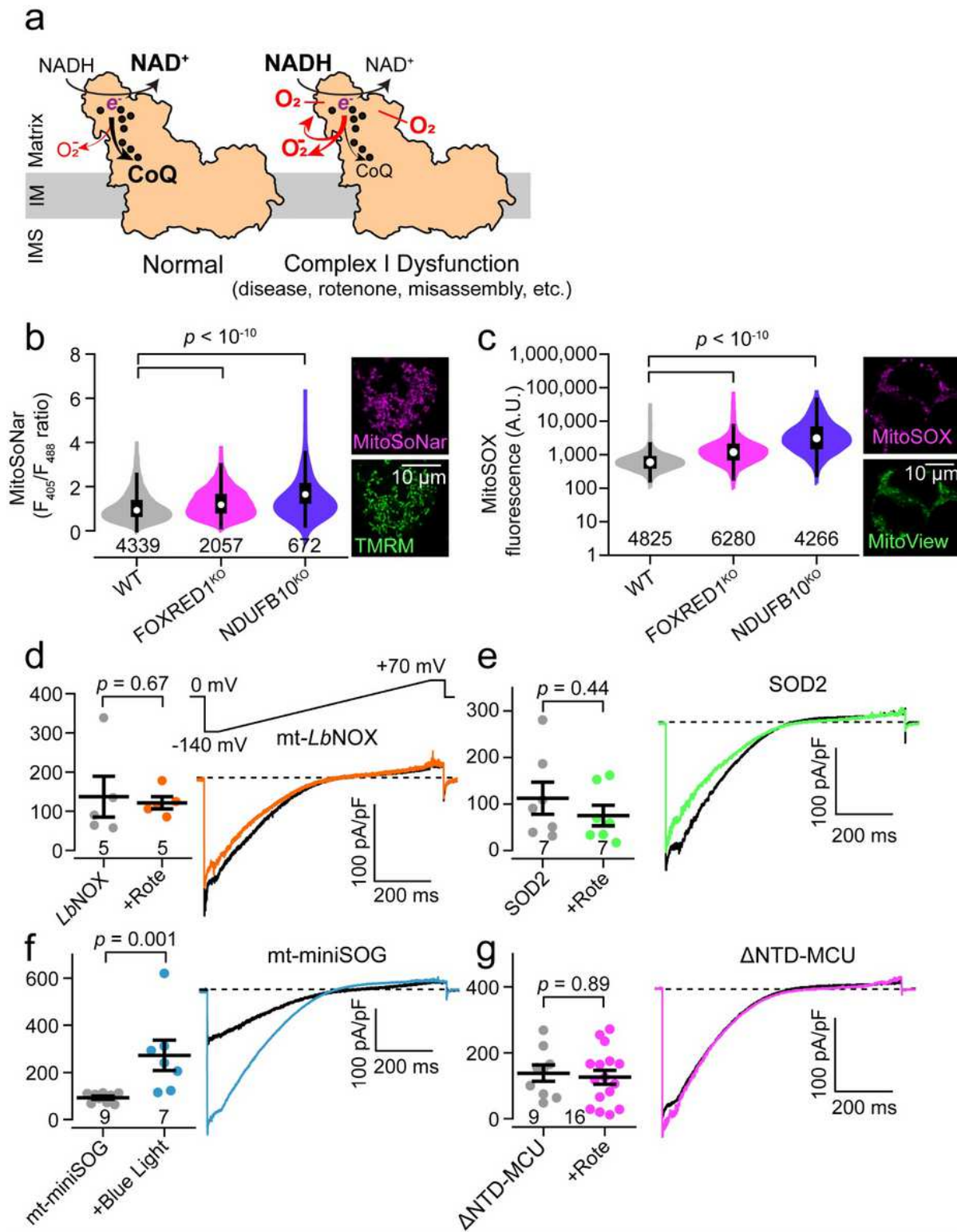


## Figure 2

Reactive oxygen species signal IMiCa enhancement. A. Complex I cartoon depicting minimal (left) and excessive (right) electron (e<sup>-</sup>) transfer from NADH to superoxide compared to ubiquinone (CoQ). Excessive O<sub>2</sub><sup>-</sup> can escape from or self-inactivate Complex I. Black dots, Fe-S clusters. IMS, intermembrane space; IM, inner membrane. B-C. Violin plots of MitoSoNar fluorescence ratio (B) and mitochondrial superoxide sensor MitoSOX fluorescence (C) measured via flow cytometry. Insets show mitochondrial targeting of the corresponding sensor. D-G. Summary (left) and exemplar (right) IMiCa in HEK293T cells expressing mito-LbNOX (D), SOD2 (E), mito-miniSOG (F), and ΔNTD-MCU (G).

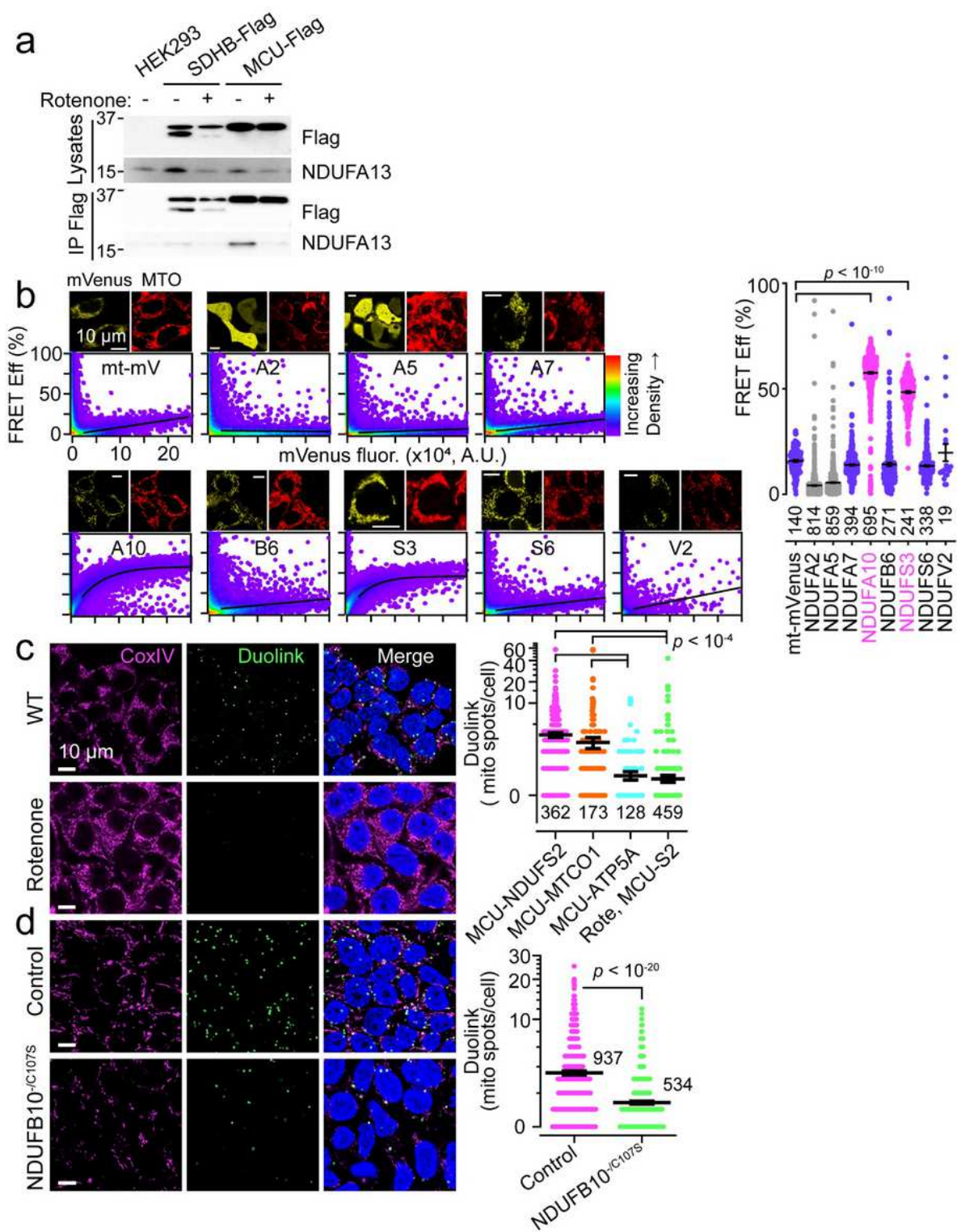


**Figure 3**

A direct interaction between MCU and Complex I alters uniporter stability. A. NDUFA13 co-immunoprecipitates with MCU-Flag. B. Left, mVenus-tagged Complex I subunits surveyed for FRET with MCU-mCerulean via flow cytometry. Images show mVenus-tagged constructs and MitoTracker Orange (MTO). Density plots display FRET efficiency against mVenus fluorescence for individual cells. Right, FRET summary. C. Left, MCU-NDUFS2 Duolink colocalization occurs in mitochondria (CoxIV) and is more

prevalent at baseline (WT) than after Complex I inhibition (Rotenone). Right, Duolink summary. Note that 74% of MCU-ATP5A and 85% of Rotenone-treated (MCU-S2) cells had zero Duolink spots, compared to 27% of MCU-NDUFS2 and 37% of MCU-MTCO1 cells. D. Left, MCU-NDUFS2 Duolink greater in control than NDUFB10-/C107S iPSCs. Right, Summary. 45% of NDUFB10-/C107S iPSCs had zero Duolink spots, compared to 19% for control.

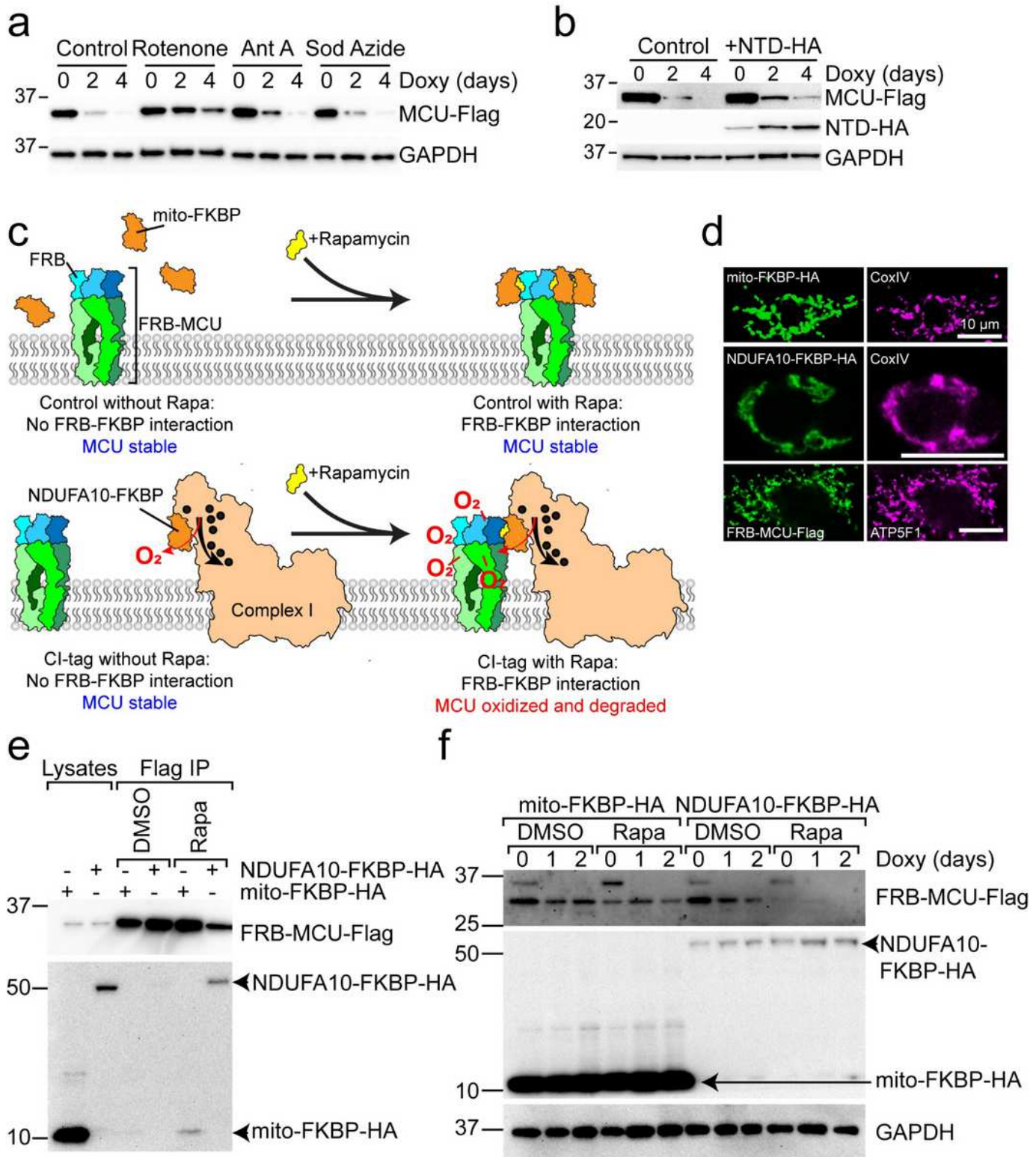
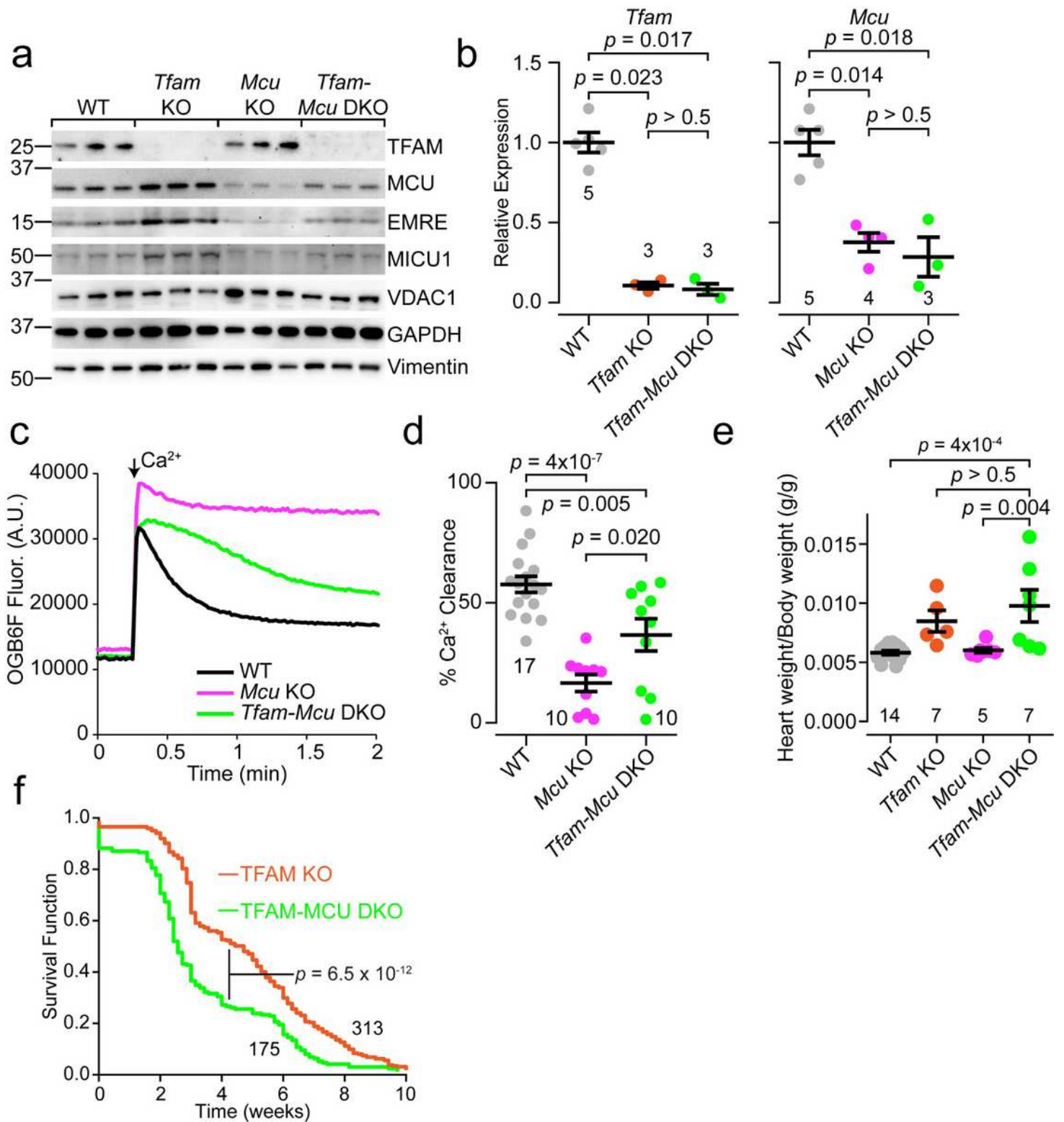


Figure 4

CLIPT controls MCU degradation. A. Doxycycline (doxy) treatment represses transcription of MCU-Flag. MCU-Flag persists after Complex I inhibition (rotenone) but not Complex III (antimycin A) or IV (sodium azide). B. MCU-Flag stabilization induced by NTD peptide. C. Design of rapamycin (Rapa)-induced dimerization experiment to test if MCU-Complex I interactions dictate MCU degradation. D. Immunocytochemistry reveals co-localization of FRB-MCU, NDUFA10-FKBP, and mito-FKBP with mitochondrial markers CoxIV or ATP5F1. E. With replacement of NTD with FRB, MCU only binds FKBP-tagged NDUFA10 in the presence of 100 nM rapamycin. Mito-FKBP-HA is a control. F. FRB-MCU is stable in the absence or presence of rapamycin when cells co-express mito-FKBP-HA control, but rapidly degraded when rapamycin induces Complex I-binding in NDUFA10-FKBP-HA expressing cells.



**Figure 5**

Diminished MCU degradation is responsible for enhanced uniporter activity in *Tfam* KO hearts, and prolongs survival. A. Immunoblotting for the specified proteins in P10-P14 mouse heart lysates. Samples from 3 mice shown per genotype. B. Analysis of *Tfam* and *Mcu* transcripts in mouse hearts. C.  $\text{Ca}^{2+}$  uptake in isolated cardiac mitochondria incubated in Oregon Green BAPTA 6F (OGB6F). Arrow indicates  $10 \mu\text{M}$   $\text{Ca}^{2+}$  pulse. D.  $\text{Ca}^{2+}$  clearance measured as the percentage of peak – baseline fluorescence

remaining after uptake of the 10  $\mu\text{M}$   $\text{Ca}^{2+}$  pulse. E. Heart weight to body weight ratios of P10-P14 mice of the indicated genotypes. F. Kaplan-Meier survival analysis of the *Tfam* KO mice compared to *Tfam*-*Mcu* DKO mice. Comparison via a log rank test.

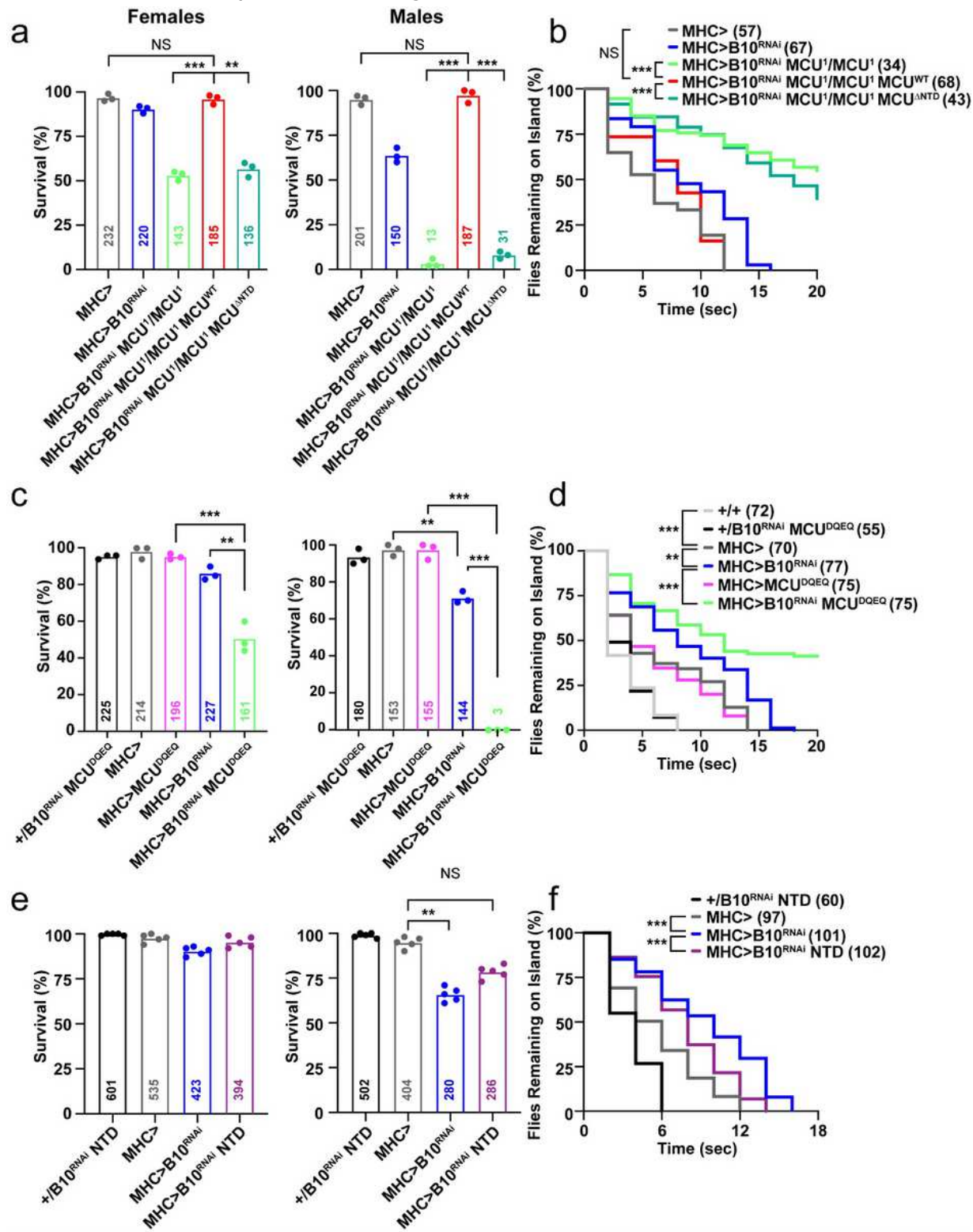


**Figure 6**

Genetic interaction between MCU and Complex I in *Drosophila*. A, C, E. *Drosophila* survival for the indicated genotypes and sex. B, D, F. Quantification of dwell time in the island assay for indicated

genotypes for female flies. A, B. The muscle specific MHC-GAL4 was used to drive expression of *NDUFB10RNAi*, *MCUWT*, or *MCUΔNTD* in wild-type or *MCU1/MCU1* mutant flies, as indicated. C, D. As in (A, B), except the dominant-negative pore mutant *MCUDQEQ* was expressed with MHC-GAL4. E, F. As in (A, B), except the isolated NTD fragment was expressed with MHC-GAL4. \*  $p < 0.05$ , \*\*  $p < 0.01$ , \*\*\*  $p < 0.001$ .

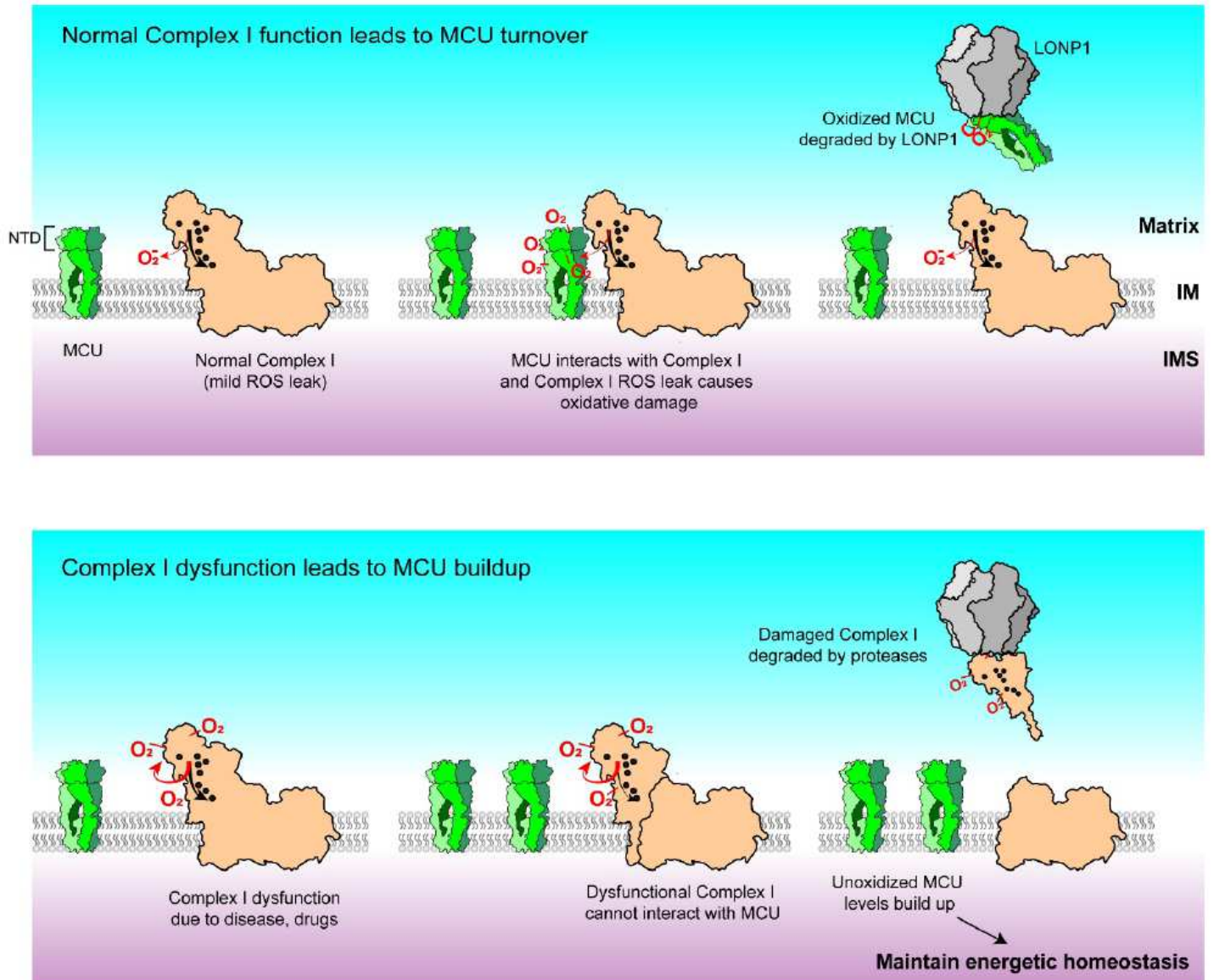


**Figure 7**

Complex I ROS controls uniporter turnover. Top, under physiological conditions, MCU interacts with Complex I and is oxidized by the mild ROS leak produced by Complex I. Such oxidized MCU becomes damaged and degraded by LONP1 or other quality-control proteases, leaving Complex I available to interact with additional channels. Bottom, when Complex I becomes impaired or misassembled, it produces excessive ROS and self-inactivates. Such dysfunctional Complex I can no longer interact with MCU, nor damage it with basal ROS leak, and is cleared by housekeeping proteases CLPP and LONP1.

Thus, functional MCU levels build up, and additional Ca<sup>2+</sup> influx through these channels maintains energetic homeostasis.

## Supplementary Files

This is a list of supplementary files associated with this preprint. Click to download.

- [S1MHCcontrol.avi](#)
- [S2MHCwithB10RNAi.avi](#)
- [S3MCU1.avi](#)
- [S4MHCwithMCU1andB10RNAi.avi](#)
- [S5MHCwithB10RNAiMCU1MCUWT.avi](#)
- [S6MHCwithMCUDQEQ.avi](#)
- [S7MHCwithB10RNAiandMCUDQEQ.avi](#)
- [S8MHCwithB10RNAiUASNTD.avi](#)
- [S9MHCwithB10RNAiMCU1dNTD1.avi](#)